Origami With Rotational Symmetry: A Review on Their Mechanics and Design

Lu Lu
Department of Mechanical Engineering,
Stanford University,
Stanford, CA 94305

Sophie Leanza
Department of Mechanical Engineering,
Stanford University,
Stanford, CA 94305

Ruike Renee Zhao[1]
Department of Mechanical Engineering,
Stanford University,
Stanford, CA 94305
e-mail: rrzhao@stanford.edu

Origami has emerged as a powerful mechanism for designing functional foldable and deployable structures. Among various origami patterns, a large class of origami exhibits rotational symmetry, which possesses the advantages of elegant geometric shapes, axisymmetric contraction/expansion, and omnidirectional deployability, etc. Due to these merits, origami with rotational symmetry has found widespread applications in various engineering fields such as foldable emergency shelters, deformable wheels, deployable medical stents, and deployable solar panels. To guide the rational design of origami-based deployable structures and functional devices, numerous works in recent years have been devoted to understanding the geometric designs and mechanical behaviors of rotationally symmetric origami. In this review, we classify origami structures with rotational symmetry into three categories according to the dimensional transitions between their deployed and folded states as three-dimensional to three-dimensional, three-dimensional to two-dimensional, and two-dimensional to two-dimensional. Based on these three categories, we systematically review the geometric designs of their origami patterns and the mechanical behaviors during their folding motions. We summarize the existing theories and numerical methods for analyzing and designing these origami structures. Also, potential directions and future challenges of rotationally symmetric origami mechanics and applications are discussed. This review can provide guidelines for origami with rotational symmetry to achieve more functional applications across a wide range of length scales. [DOI: 10.1115/1.4056637]

Keywords: origami, rotational symmetry, geometric design, deployable structures, foldable structures

1 Introduction

Origami is an ancient art of paper folding that can transform two-dimensional (2D) flat sheets into three-dimensional (3D) structures [1]. Folded configurations of origami structures are dependent on their crease patterns, which typically consist of repeated polygonal cells connected by mountain and valley creases. With rationally designed crease patterns, origami structures can achieve not only diverse folded configurations, but also various unique mechanical properties, such as bistability [2–5], multistability [6–8], negative Poisson's ratio [9–11], high load-carrying capacity [12–14], and high energy absorption efficiency [15,16]. More importantly, these properties can be tuned through the folding and reconfiguration of the origami structure. Benefitting from these features and properties, origami has been combined with modern science, leading to the field of engineering origami, which has gone far beyond art and esthetic, finding widespread applications in various fields in recent decades, including foldable architectural structures [17–20], deployable biomedical devices [21–24], shape-morphing soft robots [25–30], reconfigurable metamaterials [31–37], deployable aerospace structures [38–40], and stretchable electronics [41–46], etc.
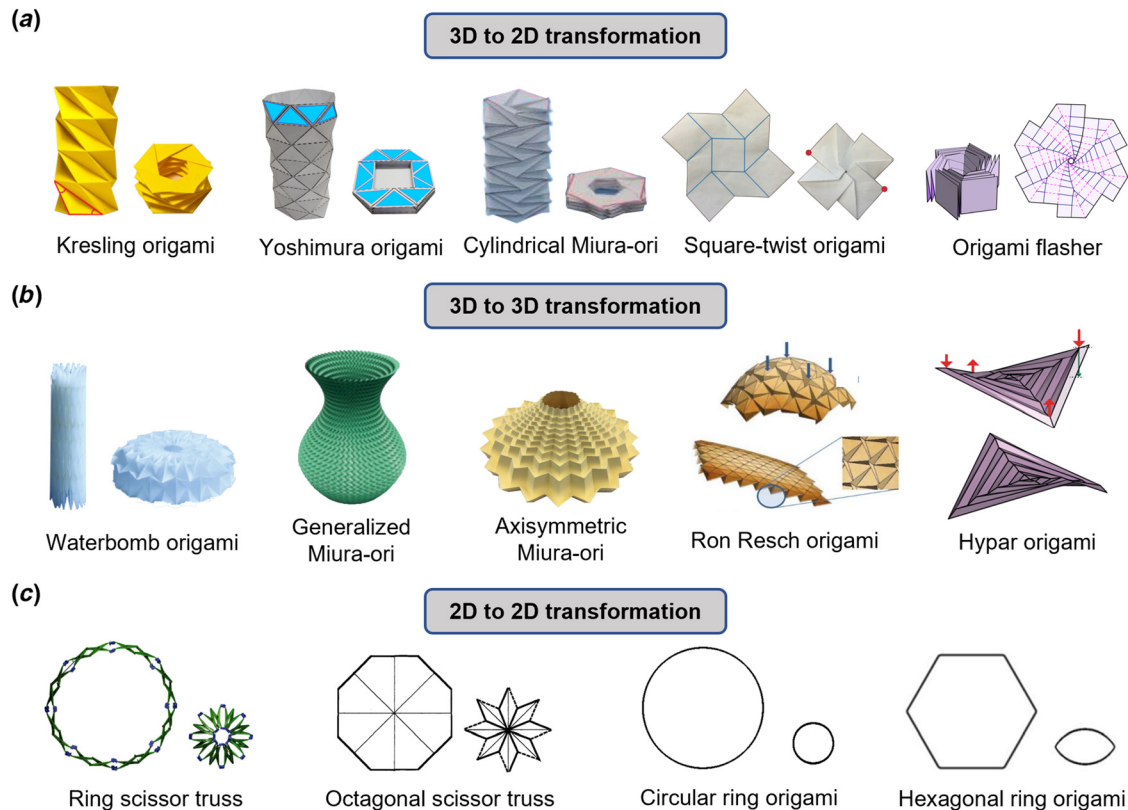
In the rich and colorful world of origami, a large set of origami possesses rotational symmetry. Typical examples include the Kresling origami [47], waterbomb origami [48], square-twist origami [49], and origami flasher [39]. Origami with rotational symmetry not only has elegant geometric shapes but also brings many useful functionalities. For instance, the waterbomb origami has a tubular configuration and can shrink and expand in the radial direction upon folding and unfolding, which has been explored for the design of medical stents [21]. The origami flasher can fold

from a large flat sheet to a stowed cylinder with significantly reduced radial size, which can be utilized for the design of portable solar panels [39]. Besides, rotationally symmetric origami has enabled many functional designs and applications across different length scales, such as spinning-enabled amphibious millirobots [50], crawling robots [51–53], transformable wheels [54,55], emergency shelters [19], foldable sunshields [56], and deployable parabolic antennas [57]. To achieve these designs and applications, a comprehensive understanding of the geometric designs and mechanical behaviors of their origami building blocks is of critical importance. Geometric designs of origami structures are usually inspired by nature [4,12,58–60] or have been developed by mathematical rules [61–64]. The folding behaviors and mechanical behaviors of origami structures, such as developability (i.e., whether the origami can be unfolded to flat), flat-foldability (i.e., whether the origami can be folded flat), and rigid-foldability (i.e., whether the origami can be folded without panel deformation), are mainly determined by the geometry of the origami. The most straightforward way to understand the relationship between the geometric designs and mechanical behaviors of origami is to analyze the energy landscape, which depicts how the elastic energy changes during the folding/unfolding process [2,5,6,65]. From the energy landscape, one can determine the number of stable states, the energy barrier that needs to be overcome for transition between stable states, and the force–displacement curve (first derivative of the energy landscape) as well as the stiffness (second derivative of the energy landscape) of the origami, etc.

In addition to classical origami based on paper folding, there are two types of foldable truss structures which also have rotational symmetry. One is the scissor truss, consisting of scissor units with two bars connected by a revolute joint, which can be designed for various 2D or 3D structures with rigid folding motions [66,67]. The second type is ring origami, formed by a closed-loop rod, which can be folded to a 2D small-volume configuration through the mechanical instability of the rod [68–70].

(a)

3D to 2D transformation

Kresling origami   Yoshimura origami   Cylindrical Miura-ori   Square-twist origami   Origami flasher

(b)

3D to 3D transformation

Waterbomb origami   Generalized Miura-ori   Axisymmetric Miura-ori   Ron Resch origami   Hypar origami

(c)

2D to 2D transformation

Ring scissor truss   Octagonal scissor truss   Circular ring origami   Hexagonal ring origami

Fig. 1 Configuration transformation of origami with rotational symmetry: (*a*) 3D to 2D transformation examples: Kresling origami (Adapted with permission from Ref. [111]. Copyright 2018, The Authors, published by National Academy of Sciences), Yoshimura origami (Adapted with permission from Ref. [125]. Copyright 2020, The Authors, published by the American Institute of Aeronautics and Astronautics), cylindrical Miura-ori (Adapted with permission from Ref. [121]. Copyright 2015 by ASME), square-twist origami (Reproduced with permission from Ref. [122]. Copyright 2015 by Springer Nature), and origami flasher (Reproduced with permission from Ref. [87]. Copyright 2016 by ASME). (*b*) 3D to 3D transformation examples: waterbomb origami (Adapted with permission from Ref. [165]. Copyright 2020, The Authors; exclusive Licensee Science and Technology Review Publishing House), generalized Miura-ori (Adapted with permission from Ref. [90]. Copyright 2016 by Springer Nature), axisymmetric Miura-ori (Adapted with permission from Ref. [73]. Copyright 2017, The Authors, published by the Royal Society), Ron Resch origami (Reproduced with permission from Ref. [14]. Copyright 2014, The Authors, published by Springer Nature), and hypar origami (Adapted with permission from Ref. [5]. Copyright 2019, The Authors, published by Springer Nature). (*c*) 2D to 2D transformation examples: ring scissor truss (Adapted with permission from Ref. [38]. Copyright 2019, The Authors, published by the American Physical Society), octagonal scissor truss (Adapted with permission from Ref. [94]. Copyright 1997 by Elsevier), circular ring origami (Reproduced with permission from Ref. [68]. Copyright 2021, The Authors, published by Wiley-VCH GmbH), and hexagonal ring origami (Reproduced with permission from Ref. [208]. Copyright 2022 by ASME).

These two kinds of foldable structures have similar folding mechanisms to the rigid-foldable origami and the non-rigidly foldable bistable origami, respectively, and can thus be considered as classes of origami without panels.

In this review, we classify origami structures with rotational symmetry into three categories, according to the dimensional changes between their deployed and folded states, as shown in Fig. 1. For the first category (Fig. 1(*a*)), the origami can be folded/unfolded from a 3D deployed configuration into a 2D flat configuration. Representative examples are the Kresling origami [47], Yoshimura origami [71], cylindrical Miura origami (Miura-ori) [47], square-twist origami [49], and origami flasher [39]. For the second category (Fig. 1(*b*)), the origami cannot be flat-folded, and can only transform between its different 3D configurations. Examples include waterbomb origami [48], generalized Miura-ori [72], axisymmetric Miura-ori [73], Ron Resch origami [74], and hypar origami [75]. For the third category (Fig. 1(*c*)), the origami can transform from one 2D configuration to another 2D configuration, which includes scissor truss structures [66] and ring origami [68]. Rigid-foldability, folding behaviors, and additional key features of these three categories of origami structures are summarized in

Table 1, from which one can have a basic understanding of origami with rotational symmetry. The outline of this review is as follows. In Sec. 2, we briefly introduce the elastic energy of classical origami based on paper folding. In Secs. 3–5, we review the geometric designs and mechanical behaviors of the three categories of origami with rotational symmetry in detail. In Sec. 6, we provide an outlook for the future of origami with rotational symmetry and outline key challenges.

2 Elastic Energy of Origami Structures

Before introducing the geometric designs and mechanical behaviors of various origami patterns, we first introduce the elastic energy of origami structures. Classical origami consists of flat panels (or facets) interconnected by the creases (or fold lines). Based on different pattern designs, origami can be rigid-foldable or non-rigidly foldable. For rigid-foldable origami, deformations only take place at the creases and the panels remain flat during folding/unfolding. Thus, the elastic energy is solely equal to the folding energy stored in the creases (U_{fold}), which can be modeled

by linear rotational springs, as shown in Fig. 2(a), and represented as [6,9,65]

$$U_{\text{fold}} = \frac{1}{2} \sum_{i=1}^{n_f} k_{f,i} \left(\theta_i - \theta_i^0 \right)^2 \tag{1}$$

where $k_{f,i}$ is the spring stiffness corresponding to the ith ($i = 1, 2, \cdots, n_f$) crease, with n_f being the number of creases. θ_i and θ_i^0 are the folding angle and the initial angle in the ith crease, respectively, which equal the dihedral angle between the two adjoining panels. Such a rotational spring model has been widely used to study mechanical behaviors of rigid-foldable origami, such as in-plane stretching stiffness of Miura-ori [9], multistability of the rigid-foldable origami building block with a degree-4 vertex (i.e., four

creases intersect at a single vertex) [6], and the bistability of the 8-crease waterbomb base [65,96].
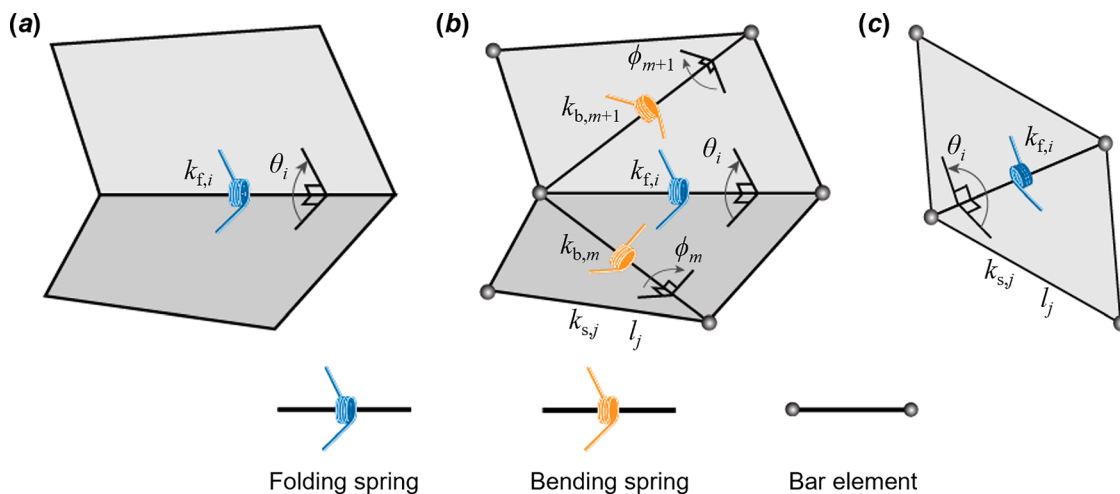
For non-rigidly foldable origami, the panels undergo in-plane stretching/shearing and out-of-plane bending, and the creases experience rotation during folding/unfolding [78,97]. Thus, the total elastic energy U_{total} of non-rigidly foldable origami includes three parts: the stretching energy U_{stretch} and the bending energy U_{bend} of the panels, and the folding energy U_{fold} at the creases, which can be written as

$$U_{\text{total}} = U_{\text{stretch}} + U_{\text{bend}} + U_{\text{fold}} \tag{2}$$

To characterize these energy components and understand the elastic behaviors of non-rigidly foldable origami, a triangulated

Table 1 Main features of origami with rotational symmetry

Configuration transformation	Origami	Rigid-foldability	Folding behavior	Folding and stability characteristics
3D to 2D	Kresling origami	No	Coupled rotation and axial contraction	Kresling origami is monostable or bistable [3,76], and the assembly of multiple Kresling units can be multi-stable [77,78]
	Yoshimura origami	Cylindrical Yoshimura origami is non-rigidly foldable [79,80]. Unclosed Yoshimura origami with an arch-like configuration is rigid-foldable [81,82]	Axial contraction	Cylindrical Yoshimura origami is monostable [79,80]
	Cylindrical Miura-ori	No	Axial contraction	Cylindrical Miura-ori is monostable or bistable [83], and its assembly can be multistable [84].
	Square-twist origami	Square-twist origami can be either rigid-foldable or non-rigidly foldable, depending on its mountain and valley crease assignment [85,86]	Coupled rotation and contraction	Rigid-foldable square-twist origami has single degree-of-freedom (DOF) motion [85]. Non-rigidly foldable square-twist origami is monostable or bistable [2]
	Origami flasher	Traditional origami flasher is non-rigidly foldable [87,88]. Rigid-foldable origami flasher can be obtained by introducing cuts or diagonal creases [39,87]	Coupled rotation and radial contraction	Traditional origami flasher exhibits bifurcation behavior during folding [38,89]
3D to 3D	Waterbomb origami	Yes	Coupled axial and radial contraction/expansion	Symmetric folding motion of water-bomb origami has a single DOF [48]
	Modified Miura-ori	Closed modified (generalized and axisymmetric) Miura-ori with rotational symmetry is non-rigidly foldable [90,91]. Unclosed modified Miura-ori is rigid-foldable [73,92]	—	Closed modified (generalized and axisymmetric) Miura-ori with rotational symmetry is not flat-foldable [90,91]. Unclosed modified Miura-ori is flat-foldable [73,92]
	Ron Resch origami	Yes	—	Rigid folding motion of Ron Resch origami has multiple DOFs [14]
	Hypar origami	No	Snap-folding	Hypar origami is bistable and has two symmetric stable states [5,93]
2D to 2D	Scissor truss	Yes	Radial contraction [94]	Scissor truss can also be designed to have 3D configurations [95]
	Ring origami	No	Snap-folding [68]	Ring origami is monostable or bistable and can be assembled to have 3D configurations [68,70]

Fig. 2 Equivalent mechanical model for rigid-foldable and non-rigidly foldable origami. (a) Rotational spring model for rigid-foldable origami. (b) Bar and hinge model for non-rigidly foldable origami with quadrilateral panels. (c) Bar and hinge model for non-rigidly foldable origami with triangular panels. Folding at the crease is modeled by the blue rotational spring, bending of the panel is modeled by the orange rotational spring, and stretching/shearing of the panel is modeled by the bar element.

truss model composed of bar elements and rotational springs [98,99], also known as the bar and hinge model [78,97,100], has been widely used. In the model, the stretching/shearing behaviors of the panels are modeled using axially deformable bars, and the folding behaviors at the creases and the bending behaviors of the panels are modeled using rotational springs. A non-rigidly foldable origami with quadrilateral panels represented by the bar and hinge model is shown in Fig. 2(b), in which the bar element along the short diagonal of each panel is introduced to model the panel bending, and thus each panel has four nodes and five bars [99]. For non-rigidly foldable origami with triangular panels, the corresponding bar and hinge model is shown in Fig. 2(c), in which the triangular panels are not further divided to capture the panel bending. Therefore, only the folding energy at the creases and the stretching energy of the panels are considered for the non-rigidly foldable origami with triangular panels [78,97]. When considering the linear elastic constitutive relation and small deformation of the origami, the stretching energy can be written as

$$U_{\text{stretch}} = \frac{1}{2} \sum_{j=1}^{n_{\text{b}}} k_{s,j} \left(l_j - l_j^0 \right)^2 \tag{3}$$

where $k_{s,j}$, l_j, and l_j^0 denote the stretching stiffness, the deformed length, and the initial length of the jth ($j = 1, 2, \cdots, n_{\text{b}}$) bar element, respectively, with n_{b} being the number of bar elements. The bending energy can be expressed as

$$U_{\text{bend}} = \frac{1}{2} \sum_{m=1}^{n_{\text{d}}} k_{b,m} \phi_m^2 \tag{4}$$

in which $k_{b,m}$ is the spring stiffness corresponding to the mth ($m = 1, 2, \cdots, n_{\text{d}}$) diagonal bar element, with n_{d} being the number of diagonal bar elements, and ϕ_m representing the bending angle of the panels. Note that the initial bending angle equals zero, as the panels are flat in the initial state. Calculation of the folding energy (U_{fold}) for non-rigidly foldable origami is identical to that of the rigid-foldable origami, as shown in Eq. (1). The spring stiffnesses used in the model can be determined by experiments.

The conventional bar and hinge model can only capture the small deformation of origami [99]. To overcome this limitation, several modified bar and hinge models have been developed in recent years [78,97,98,100]. For example, Liu and Paulino [78] developed a general nonlinear framework for the bar and hinge model by considering nonlinear constitutive relations for the bars
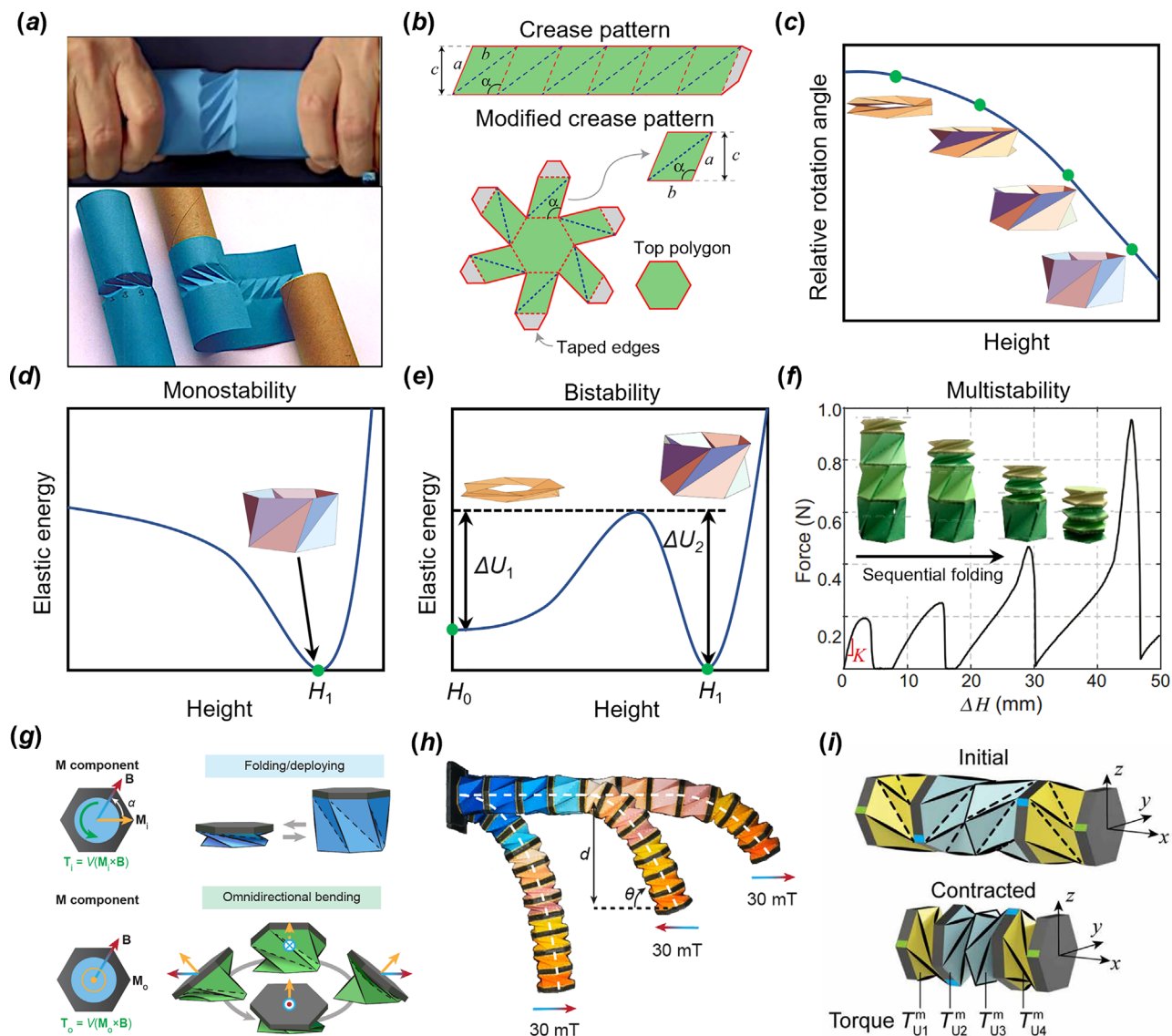
and springs, which can capture the large deformation of non-rigidly foldable origami. Filipov et al. [97] modified the bar and hinge model by introducing two diagonal bar elements and their intersection node for each quadrilateral panel as well as incorporating nonlinear constitutive relations, which has proven to be capable of capturing symmetric and isotropic in-plane behaviors of non-rigidly foldable origami. These bar and hinge models can quantitatively capture the key characteristics of origami structures such as folding kinematics, bistability, and multistability, while they cannot capture the localized behaviors such as crease buckling, panel buckling, and stress concentrations [78,97,101]. By using these bar and hinge models, the mechanical behaviors of various origami structures have been widely studied, which will be discussed in subsequent sections.

3 3D-To-2D Origami With Rotational Symmetry

Next, we introduce the geometric designs and mechanical behaviors of origami with rotational symmetry that can be folded/unfolded from a 3D configuration to a 2D configuration. This category of origami usually has significant packing abilities, and thus has great application potential in the design of deployable architectural and aerospace structures. Here, we introduce five common types of origami with rotational symmetry, which are the Kresling origami, Yoshimura origami, cylindrical Miura-ori, square-twist origami, and origami flasher.

3.1 Kresling Origami. Kresling origami is one very popular example of origami with rotational symmetry. It was originally discovered by the architect Biruta Kresling when performing twist buckling experiments of a thin-walled paper cylinder [47,102], as shown in Fig. 3(a). The Kresling pattern is composed of a series of congruent parallelogram unit cells containing diagonal creases (Fig. 3(b) [77]), which form a cylindrical configuration by folding along the mountain (red) and valley (blue) creases and connecting the two ends. Alternatively, it can be constructed by using a flower-like crease pattern [103], which replaces the mountain creases with cuts (Fig. 3(b)). The geometry of the Kresling pattern is characterized by four parameters: the side lengths a and b, the sector angle α, and the number of the parallelogram unit cells n. Kresling origami can be either monostable or bistable, depending on its geometric parameters as well as the material of the flat sheet. For a bistable Kresling origami, it has a deployed stable state and a folded stable state, and the two stable states have

Fig. 3 Geometric design and mechanical behaviors of Kresling origami. (*a*) Twist buckling of a thin-walled paper cylinder (Reproduced with permission from the author [47,102]). (*b*) Crease pattern and modified crease pattern of Kresling origami. The red dashed lines denote the mountain creases, and the blue dashed lines denote the valley creases. (Reproduced with permission from Ref. [77]. Copyright 2020 by National Academy of Sciences) (*c*) Coupled axial and rotational deformation of Kresling origami. (d,e) Energy landscapes of (*d*) monostable Kresling origami and (*e*) bistable Kresling origami. Green dots represent the positions of the stable states. (*f*) Force-displacement curve of a four-unit Kresling assembly with units of different heights (Adapted with permission from Ref. [77]. Copyright 2020 by National Academy of Sciences). (*g*) Magnetic actuation for folding/deploying and omnidirectional bending of Kresling origami [26]. (*h*) Magnetically actuated contraction/stretching/ bending of a Kresling robotic arm (Figures (*g*) and (*h*) are adapted with permission from Ref. [26]. Copyright 2021, The Authors, published by National Academy of Sciences). (*i*) Magnetically actuated pure translational deformation and simultaneous contraction of a rationally designed Kresling assembly with units of reverse crease directions. The units at the two ends have a crease direction opposite to that of the units in the middle (Reproduced with permission from Ref. [51]. Copyright 2022, The Authors, some rights reserved; exclusive licensee American Association for the Advancement of Science).

different heights and different relative rotation angles between their top and bottom surfaces. During folding/unfolding, the relative rotation angle varies with the height of the Kresling origami, demonstrating a coupled axial and rotational deformation, as shown in Fig. 3(*c*).

Two common types of energy landscapes of Kresling origami are illustrated in Figs. 3(*d*) and 3(*e*), which are the cases of monostability and bistability, respectively. As can be seen, the energy landscape of a monostable Kresling origami has only one energy minimum (Fig. 3(*d*)), corresponding to its sole stable state. The energy landscape of a bistable Kresling origami has two energy minima (Fig. 3(*e*)), corresponding to its stable folded (with height
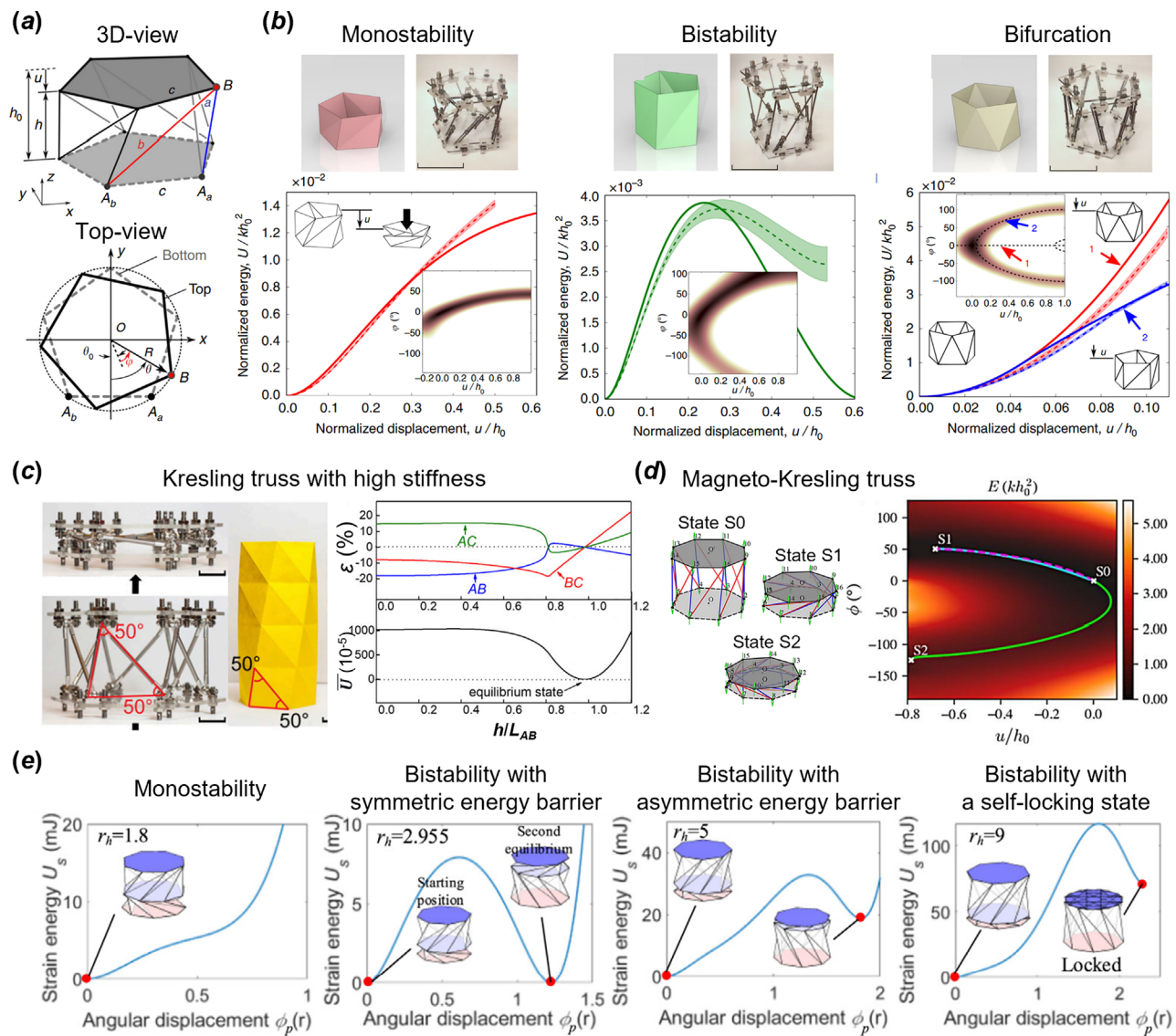
H_0) and deployed (with height H_1) states. The height of the folded stable state can be either zero ($H_0 = 0$) or nonzero ($H_0 \neq 0$), depending on the geometric design. An energy barrier needs to be overcome in order to transition between the two stable states. Particularly, the energy barrier (ΔU_2) required to go from the deployed stable state to the folded stable state is higher than that required to switch back (ΔU_1) since the creases store energy in the folded stable state.

By assembling multiple Kresling units of the same cross section, Kresling origami can exhibit multistability. Figure 3(*f*) shows the force–displacement curve of a Kresling assembly composed of four bistable units, with each unit having a different stable

deployed height [77]. Upon axial loading, the Kresling assembly snap-collapses in a sequential manner, starting from the top unit and ending with the bottom unit, due to the increasing stable height of each unit down the assembly. Such sequential folding behavior is independent of the stack order of the Kresling units [103] and only relies on the energy barrier of each individual unit. Since each Kresling unit has a distinct stiffness (represented by the slope K of the force–displacement curve), the global stiffness of the Kresling assembly can be programmed by selectively controlling the folded/deployed state of each unit. For a Kresling assembly with N different bistable units, it can exhibit 2^N independent stable states, corresponding to 2^N different stiffnesses [77].

By harnessing the bistability of Kresling origami, a variety of functional designs and applications have been achieved, such as impact mitigation systems [104], robotic arms [105], crawling robots [52], frequency-reconfigurable antennas [106,107], and mechanical memory operations [108,109]. However, the functionalities of these applications are commonly achieved through a mechanical or pneumatic actuation, which relies on either slow, tethered, or bulky actuators (or a combination). Recently, Zhao group [26,50,51,77] proposed a robust, untethered, and distributed actuation strategy for Kresling origami through magnetic control. The magnetic actuation is accomplished by the torque generated from the soft magnetic-responsive plate attached to the polygon end of the Kresling origami, as shown in Fig. 3(g). For a magnetic plate with a magnetization $\mathbf{M}$ under a magnetic field $\mathbf{B}$, the resulting torque $\mathbf{T}$ is given by $\mathbf{T} = V(\mathbf{M} \times \mathbf{B})$, with V being the volume of the magnetic plate. Therefore, the direction and magnitude of the magnetic torque can be controlled by programming the magnetization of the attached plate as well as by adjusting the direction and intensity of the external magnetic field. Figure 3(g)

Fig. 4 Mechanical behaviors of Kresling trusses. (a) Schematic of a Kresling truss composed of rigid polygons and elastic truss members [108]. (b) Energy landscapes of Kresling trusses exhibiting monostability, bistability, and bifurcation behaviors (Figures (a) and (b) are adapted with permission from Ref. [108]. Copyright 2017, The Authors, published by Springer Nature). (c) Strain and normalized energy versus normalized height of a monostable Kresling truss with high stiffness (Adapted with permission from Ref. [111]. Copyright 2018, The Authors, published by National Academy of Sciences). (d) Contour plot for energy of a magneto-Kresling truss with three stable states (Reproduced with permission from Ref. [117]. Copyright 2021 by ASME). (e) Energy landscapes of Kresling truss assemblies with monostability, bistability with symmetric energy barrier, bistability with asymmetric energy barrier, and bistability with a self-locking state (Reproduced with permission from Ref. [112]. Copyright 2020 by Elsevier).

shows that designing the magnetization direction can program the torque direction to achieve different deformation modes of the single Kresling unit: an in-plane torque leads to folding/deploying, while an out-of-plane torque leads to bending [26]. This actuation strategy has enabled the design of a magnetically controlled robotic arm that is capable of integrated multimodal deformations of contraction, stretching, omnidirectional bending, and twisting [26], as shown in Fig. 3(h). By assembling four Kresling units with the same geometry and reverse crease directions, and rationally designing the magnetizations of four attached magnetic plates, the resulting Kresling assembly can achieve pure translational deformation and simultaneous contraction, as shown in Fig. 3(i), which has been used for the design of a small-scale and untethered robot with both crawling and steering capabilities [51]. Besides, Kresling origami combined with the proposed magnetic actuation strategy has enabled functional applications such as logic circuits capable of digital computing [77] and multifunctional wireless amphibious millirobots with capabilities of multimodal locomotion, drug delivery, and cargo transportation [50].

When removing the panels of Kresling origami and replacing the creases with elastic truss members, a Kresling truss can be obtained [108,110]. As shown in Fig. 4(a) [108], the top and bottom surfaces of a Kresling truss are rigid regular polygons circumscribed by circles of radius R, which have an initial height h_0 and a relative rotation angle θ_0 between them. The truss members corresponding to the mountain and valley creases have initial lengths a_0 and b_0, respectively. During folding/unfolding, the top and bottom surfaces always share the same rotational axis, and the truss members only deform axially. Thus, Kresling trusses only have two DOFs (one translational and one rotational), and their elastic energy can be written as [108]

$$U_K = \frac{1}{2}nk(a - a_0)^2 + \frac{1}{2}nk(b - b_0)^2 \tag{5}$$

where n is the side number of the top/bottom regular polygon, k is the stiffness of the truss member, and a and b are the lengths of the truss members corresponding to the mountain and valley creases during the folding process, respectively, which are given by

$$a = \sqrt{(h_0 - u)^2 + 4R^2 \sin^2\left(\frac{\varphi}{2} + \frac{\theta_0}{2} - \frac{\pi}{2n}\right)} \tag{6}$$

$$b = \sqrt{(h_0 - u)^2 + 4R^2 \sin^2\left(\frac{\varphi}{2} + \frac{\theta_0}{2} + \frac{\pi}{2n}\right)} \tag{7}$$

Here, u and φ are the axial and rotational displacements, respectively. Note that φ should be less than $\pi - \pi/n - \theta_0$ [108], otherwise the truss members will intersect each other.

Based on the 2-DOF truss model and its modified versions, stability characteristics of Kresling trusses have been widely studied [76,108,111–113]. Yasuda et al. [108] studied the energy landscapes of Kresling trusses exhibiting monostability, bistability, and bifurcation characteristics based on a modified 2-DOF truss model. It can be seen from Fig. 4(b) that the monostable Kresling truss has only one energy minimum located at the initial state, therefore its elastic energy increases monotonically when subjected to an axial compressive force during the folding process. For a bistable Kresling truss, there are two zero-energy minima in the energy landscape, which correspond to the deployed stable state and the folded stable state, respectively. Unlike bistable Kresling origami with an asymmetric energy barrier, the Kresling truss experiences the same energy barrier during the transition between its two zero-energy stable states. Additionally, the Kresling truss can undergo bifurcation when the initial relative rotation angle between the top and bottom surfaces equals zero ($\theta_0 = 0$). In this case, the truss is axially compressed without rotation in the

initial stage. When reaching the bifurcation point, a pitchfork bifurcation behavior is observed, as shown in the inset, which has three branches: one unstable branch and two stable branches. On the unstable branch, the truss continues to be axially compressed without rotation (path indicated by the arrow 1). On the two stable branches, the axial motion is coupled with rotational motion (path indicated by the arrow 2). Note that, by additionally taking off-axis deformation into account, the 2-DOF truss model can be extended to a 6-DOF truss model, which has been utilized to study the dynamics of Kresling trusses [114,115].

Kresling trusses can be designed to be either stiff or flexible by rationally selecting the geometry of the unit cells. When the Kresling truss is monostable, its stiffness is relatively high. For example, Zhai et al. [111] studied the mechanical behavior of a monostable Kresling truss as shown in Fig. 4(c), and found that the maximum strain in the truss members exceeds 10% when compressing the Kresling truss from the equilibrium state to its collapsed state. In comparison, when the Kresling truss is bistable, the maximum strain undertaken by the truss members can be less than 1% before collapsing to its other stable state [111]. The stiffness can be further decreased, particularly when the initial relative rotation angle between the top and bottom surfaces equals $\pi/2$, where the Kresling truss exhibits a zero-stiffness mode [108]. In this case, axial compression in the initial stage does not require large axial force or torque, thus the elastic energy slowly grows to be extreme, which has been used for the design of vibration isolators [116]. Moreover, Yang and Keten [117] found that the stability of Kresling origami can be altered by embedding magnetic dipoles at each vertex of its top and bottom polygons in an alternating fashion. As shown in Fig. 4(d), a monostable Kresling truss becomes tri-stable due to interactions between the embedded magnets, exhibiting one deployed stable state S0 and two collapsed stable states S1 and S2. Additionally, Li et al. [112] found that Kresling trusses with identical top and bottom polygons but opposite directions of creases can be assembled to achieve diverse stability characteristics. As shown in Fig. 4(e), two-unit Kresling truss assemblies with different initial top unit to bottom unit height ratios (r_h) can have monostability, bistability with symmetric energy barrier, bistability with asymmetric energy barrier, or bistability with a self-locking state [112].

In addition to traditional Kresling origami, the Kresling pattern can be modified to realize more functional designs. As shown in Fig. 5(a) [118], by replacing the parallelogram unit cells of the traditional Kresling pattern with general quadrilateral ones, conical Kresling origami can be constructed [118–120]. The geometry of the conical Kresling pattern is defined by five parameters (a, b, c, β, n), with a, b, c, and β being the geometric parameters of the quadrilateral unit cells and n being the number of the quadrilateral unit cells. Conical Kresling origami preserves the key characteristics of traditional Kresling origami, which means that it also has coupled axial and rotational deformation and is capable of bistability. Figure 5(b) shows the contour map of the energy barrier of bistable conical Kresling origami with respect to the edge length ratio (a/b) and the deployed stable height h_1 [118]. It is seen that the energy barrier decreases with the increasing edge length ratio, while it increases with increasing stable-state height. Therefore, the energy barrier of a conical Kresling origami is higher than that of a traditional Kresling origami ($a/b = 1$) of the same stable height. Benefitting from the enlarged design space of general quadrilateral unit cells, conical Kresling origami can be assembled to approximate 3D surfaces of revolution with various types of Gaussian curvatures. As shown in Fig. 5(c), the fully deployed stable states of conical Kresling assemblies can approximate hyperboloid of revolution with negative Gaussian curvature, ellipsoid of revolution with positive Gaussian curvature, and vase-shaped sinusoid of revolution with mixed curvature [118]. The fully folded stable states allow these assemblies to be packed into small-volume configurations.

Moreover, Ishida et al. [121] proposed a toroidal Kresling origami which can be used to construct a deployable torus. The
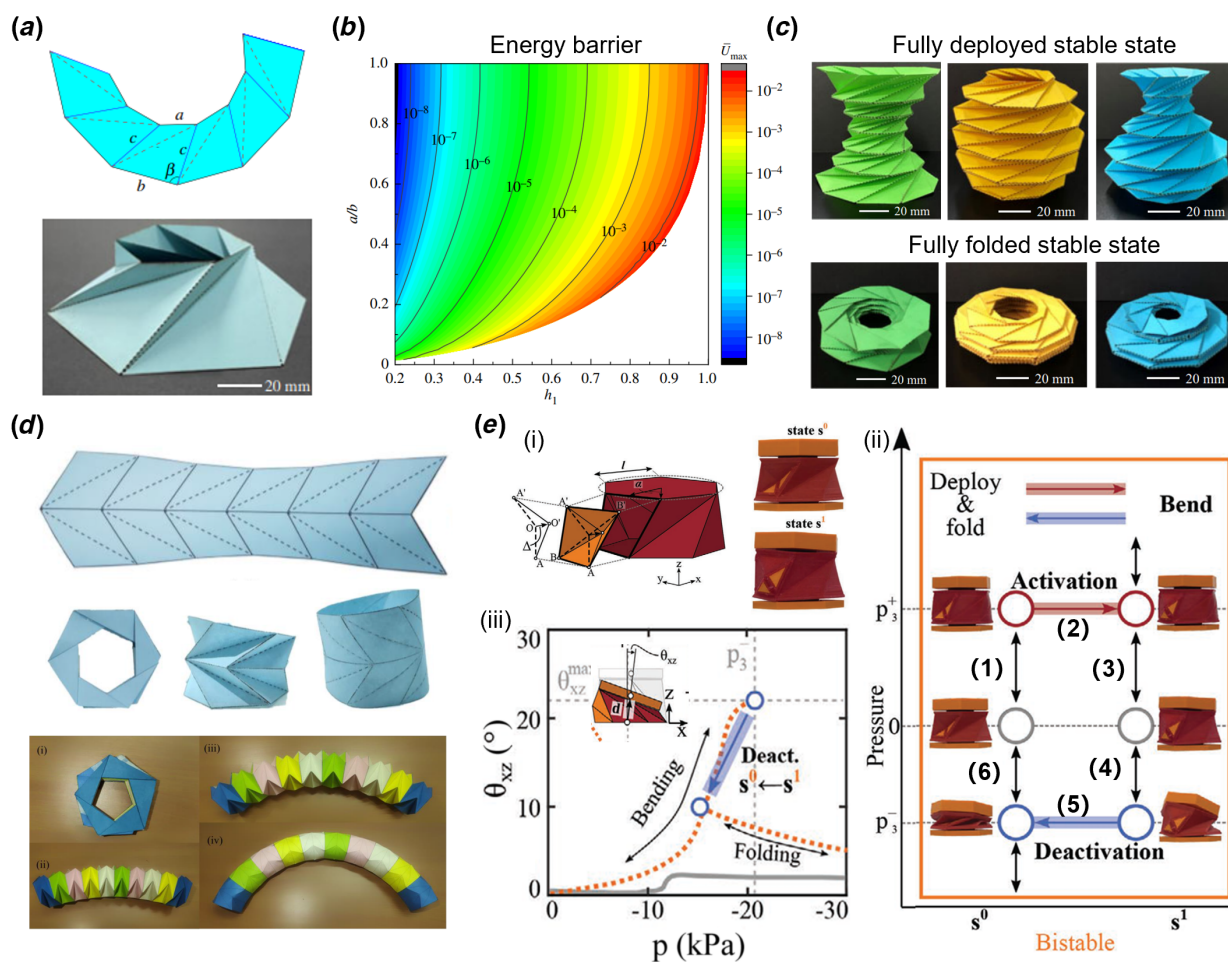
toroidal Kresling pattern is composed of two arrays of trapezoidal unit cells with diagonal creases [123], as shown in Fig. 5(d). With rationally designed geometric parameters, the toroidal Kresling origami can be flat-folded, partially folded, or fully deployed to a segment of a torus. By connecting multiple segments of the toroidal Kresling units, a circumferentially foldable toroidal tube can be obtained [123]. Recently, Melancon et al. [124] modified the Kresling pattern by introducing two additional valley creases (effectively four creases) to one of its panels (see Fig. 5(e-i)), which turns a monostable Kresling unit into a bistable one. In the stable state s^0, all panels are folded inward. In the stable state s^1, the modified panel is popped outward, but all other panels are still folded inward. The stable state transition can be achieved through pneumatic actuation. As shown in Fig. 5(e-ii), upon inflation to a critical pressure (step 1), the modified Kresling origami snaps (step 2) from state s^0 to state s^1. The origami can transit back to s^0 from state s^1 by deflating (steps 3 and 4) the origami unit until bending and eventually inward panel snapping (step 5) at a critical negative pressure to a flat state occurs, followed by inflation (step 6). Variation of the bending angle with the pressure during deflation is shown in Fig. 5(e-iii), with the maximum bending angle determined by when the top and bottom caps contact. By

assembling multiple such inflatable Kresling units with different snapping pressure thresholds, the structure can shape-shift to different target deformation modes using only one pressure input [124].

3.2 Yoshimura Origami. Yoshimura origami is another cylindrical origami with rotational symmetry that can be folded into a 2D configuration, which was discovered from the post-buckling of thin cylindrical shells under axial loading [71]. As shown in Fig. 6(a), the Yoshimura pattern is composed of identical isosceles triangles, and its geometry can be defined by two parameters: the side length a and the apex angle θ [79,125]. By folding along the creases and connecting the two ends, cylindrical Yoshimura origami can be obtained, and its rotational symmetry order depends on the number of unit cells in the circumferential direction, such as the examples shown in Fig. 6(a), which have 8, 6, 4, and 3-fold rotational symmetry, respectively [80].

Unlike Kresling origami, which possesses bistability and coupled axial and rotational deformation, Yoshimura origami has only one stable state (i.e., initial configuration), and only produces axial contraction under axial compression [79,80,125]. The axial stiffness of Yoshimura origami is very high and therefore requires

Fig. 5 Geometric design and mechanical behaviors of modified Kresling origami. (*a*) Crease pattern and folded configuration of conical Kresling origami [118]. The dashed lines represent the valley creases, and the blue solid lines denote the mountain creases. (*b*) Contour map of the energy barrier of bistable conical Kresling origami with respect to the deployed stable height and the edge length ratio [118]. (*c*) Conical Kresling origami assemblies that can approximate 3D surfaces of revolution with different Gaussian curvatures (Figures (*a*)–(*c*) are adapted with permission from Ref. [118]. Copyright 2022, The Authors, published by the Royal Society). (*d*) Crease pattern, folded configuration, and assembly of toroidal Kresling orgami (Reproduced with permission from Ref. [123]. Copyright 2022 by Elsevier). The dashed lines represent the valley creases, and the solid lines denote the mountain creases (*e*) Schematic and experimental model (i), stable state transition diagram (ii), and bending angle versus pressure graph (iii) of inflatable Kresling origami with one panel containing four creases (Reproduced with permission from Ref. [124]. Copyright 2022 by Wiley-VCH GmbH).
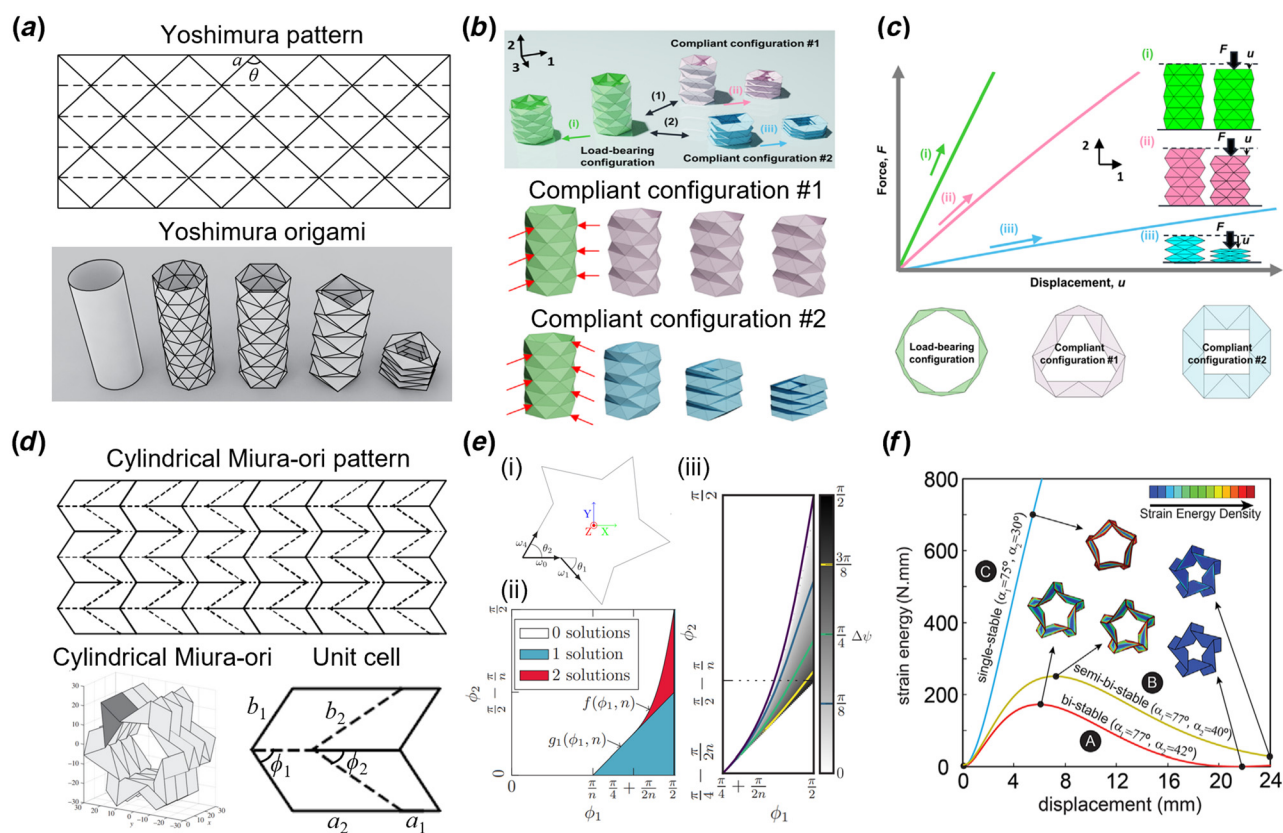
a large compressive force to be folded. Recently, Suh et al. [79,125] found that a cylindrical Yoshimura origami could be reconfigured into two different derivative compliant configurations with much lower stiffness by squeezing a specific combination of vertices to face inward, as shown in Fig. 6(b), with their cross-sectional shapes illustrated in the bottom row of Fig. 6(c). Compliant configuration 2 indicated in the figure, also known as the accordion pattern or bellows pattern, consists of isosceles trapezoids [125]. Figure 6(c) shows the force–displacement curves of the Yoshimura origami and its two derivatives [79]. It is seen that, for the three different configurations, axial forces increase almost linearly with the displacement during the folding process. In particular, the axial stiffness of Yoshimura origami is much higher than its two derivative patterns, meaning that the two derivative patterns are easier to fold than Yoshimura origami. By harnessing the mechanical properties and folding behaviors, Yoshimura origami and its derivatives have been widely used for energy absorption devices [16], worm-like crawling robots [126], soft pneumatic actuators [127], and shape-morphing grippers [60,128]. Note that the Yoshimura pattern can also be folded into an unclosed arch-like configuration [81]. In this case, the Yoshimura origami is rigid-foldable with multiple DOFs [82,129], which is commonly used for the design of deployable shelters [130,131].
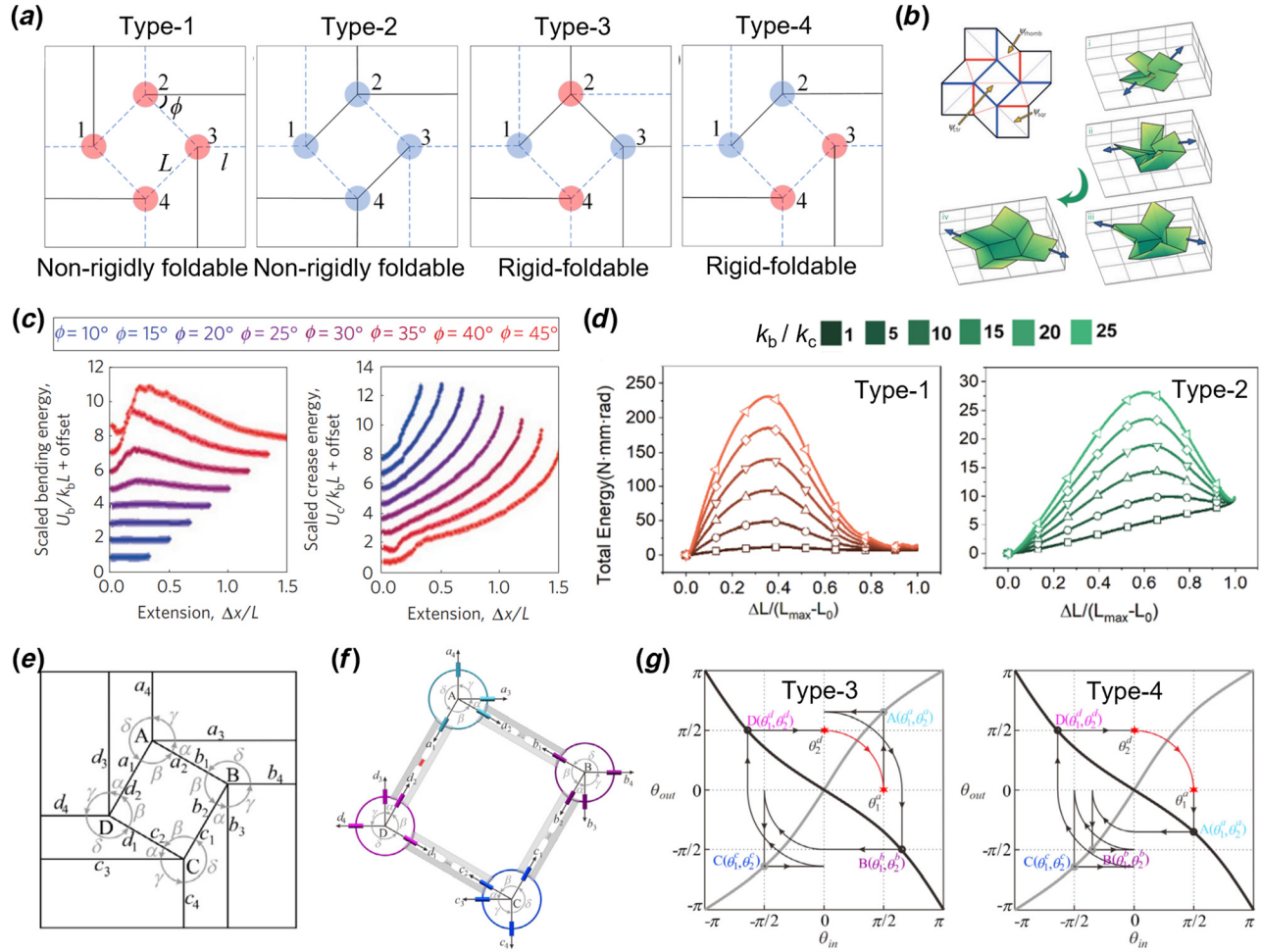
3.3 Cylindrical Miura Origami. Miura-ori is the most well-known classical origami pattern, which has attracted significant

attention from engineering and science communities since it was first proposed by Koryo Miura for packaging and deployment of large membranes in space [132]. A standard Miura-ori pattern is composed of repeated parallelograms, which form a corrugated planar tessellation not only capable of significant packing when folded, but also of diverse impressive properties such as developability, flat-foldability, rigid-foldability, single DOF motion, and negative Poisson's ratio [9,133]. By utilizing these properties, Miura-ori have enabled various functional designs, including mechanical metamaterials with tunable properties [35,36,134], shape-morphing soft robots [60], artificial muscles [135], deployable architecture [17], and deformable energy storage devices [136,137], etc.

Standard Miura-ori is rigid-foldable and exhibit in-plane folding motion. However, when the valley creases (dashed lines in Fig. 6(d)) on the two sides of a collinear crease are not parallel to the edge creases, the modified Miura-ori pattern can be folded into a closed-loop configuration with rotational symmetry, i.e., the cylindrical Miura-ori [47,138–141], as shown in Fig. 6(d) [138]. The geometry of the unit cell of cylindrical Miura-ori is defined by six parameters: the side lengths a_1, a_2, b_1, b_2, and the sector angles ϕ_1 and ϕ_2, with $0<\phi_2<\phi_1<\pi/2$. To obtain a rotationally symmetric cylindrical configuration, the two angles θ_1 and θ_2 of the closed-loop configuration (see Fig. 6(e-i)) formed by the collinear creases must satisfy the following equation [83]

Fig. 6 Geometric designs and mechanical behaviors of Yoshimura origami and cylindrical Miura-ori. (a) Crease pattern (top) and folded configurations (bottom) of Yoshimura origami (Bottom: reproduced with permission from the authors [80]). The dashed lines represent the valley creases, and the solid lines denote the mountain creases. (b) Two derivative configurations of Yoshimura origami [79]. (c) Force-displacement curves of Yoshimura origami and its two derivative configurations (Figures (b) and (c) are adapted with permission from Ref. [79]. Copyright 2022 by Wiley-VCH GmbH). (d) Crease pattern, folded configuration, and unit cell of cylindrical Miura-ori. The dashed lines represent the valley creases, and the solid lines denote the mountain creases. (Adapted with permission from Ref. [138]. Copyright 2015, The Authors, published by the Royal Society). (e) Closed-loop formed by the collinear creases (i), phase-diagram for the geometric design (ii), and contour plot for the angle difference between the deployed and collapsed stable states (iii) of cylindrical Miura-ori (Adapted with permission from Ref. [83]. Copyright 2017 by American Physical Society). (f) Energy landscapes of cylindrical Miura-ori with different stability characteristics (Reproduced with permission from Ref. [84]. Copyright 2018 by WILEY-VCH Verlag GmbH & Co. KGaA, Weinheim).

Fig. 7 Geometric design and mechanical behaviors of square-twist origami. (*a*) Four typical crease patterns of the square-twist origami. The dashed lines represent the valley creases, and the solid lines denote the mountain creases. (Reproduced with permission from Ref. [146]. Copyright 2021 by Elsevier). (*b*) Unfolding process of type-1 square-twist origami consisting of square and rhombus panels [2]. (*c*) Bending energy and folding energy versus displacement of type-1 square-twist origami (Figures (*b*) and (*c*) are reproduced with permission from Ref. [2]. Copyright 2015 by Springer Nature). (*d*) Energy landscapes of type-1 and type-2 square-twist origami (Adapted with permission from Ref. [86]. Copyright 2022 by Elsevier). (*e*) Schematic of the square-twist pattern with geometric description [85]. (*f*) Equivalent four spherical 4R linkages for rigid-foldable square-twist pattern [85]. (*g*) Kinematic motion transmission paths of type-3 and type-4 square-twist origami (Figures (*e*)–(*g*) are reproduced with permission from Ref. [85]. Copyright 2022 by Elsevier).

$$\theta_1 + \theta_2 = \pi - \frac{2\pi}{n} \tag{8}$$

in which n is the number of unit cells in the circumferential direction, and $n \geq 3$. Moreover, the angle θ_1 and the opening angle ψ of the panel can be expressed in terms of the sector angles ϕ_1 and ϕ_2 of the unit cell as [83]

$$\tan\frac{\theta_1}{2} = \frac{1}{2\tan\frac{\pi}{n}} \left[1 - \frac{\tan\phi_2}{\tan\phi_1} \pm \sqrt{\left(\frac{\tan\phi_2}{\tan\phi_1} - 1\right)^2 - 4\frac{\tan\phi_2}{\tan\phi_1}\tan^2\frac{\pi}{n}} \right] \tag{9}$$

$$\sin\psi = \frac{\tan(\theta_1/2)}{\tan\phi_2} \tag{10}$$

Note that θ_1 must be less than $\pi - 2\pi/n$ to avoid self-intersection of the panels. Based on Eqs. (9) and (10), Reid et al. [83] plotted a phase diagram for the geometric design of cylindrical Miura-ori, which is shown in Fig. 6(*e*-ii). It is seen that the sector angles

have one or two solutions, which means that cylindrical Miura-ori can be either monostable (blue region) or bistable (red region). On the line $g_1(\phi_1, n)$, the two sector angles satisfy $\phi_1 - \phi_2 = \pi/n$, and the cylindrical Miura-ori is flat-folded. When $\phi_1 \leq \pi/4 + \pi/(2n)$, the bistable region disappears and the cylindrical Miura-ori can only be monostable. For bistable cylindrical Miura-ori, the contour map in Fig. 6(*e*-iii) illustrates the angle difference $\Delta\psi$ between the collapsed and deployed stable states [83], which represents the "deployability" of the cylindrical Miura-ori, with respect to different sector angles ϕ_1 and ϕ_2. At the boundary point $(\phi_1, \phi_2) = (\pi/2, \pi/2 - \pi/n)$, the collapsed state is flat-folded and the deployed state is completely extended, thus the cylindrical Miura-ori with $\Delta\psi = \pi/2$ represents a design with maximum deployability. As the sector angles move away from the boundary point, the deployability of the cylindrical Miura-ori monotonically decreases.

The cylindrical Miura-ori is not rigidly foldable, as the folding motion can only be achieved when panel deformation is allowed [140,142]. Kamrava et al. [84] studied the energy landscapes of three different cylindrical Miura-ori illustrated in Fig. 6(*f*), which exhibit monostable, semi-bistable, and bistable behaviors, respectively. For the monostable cylindrical Miura-ori, the strain energy monotonically increases with the displacement, and its single

stable configuration is in the initial state. For the semi-bistable case, when the displacement increases, the strain energy first increases to the maximum and then decreases to a nonzero energy state where the panels are in contact. For the bistable cylindrical Miura-ori, its energy landscape has two zero-energy states, corresponding to the collapsed and deployed stable states. The energy barrier associated with the transition between the two stable states increases as the circumferential unit cell number n increases [84]. Bistable cylindrical Miura-ori units can serve as building blocks to construct cellular metamaterials with anisotropic multistability [84]. Moreover, with carefully considered geometric parameters, cylindrical Miura-ori can be designed to have different cross section shapes [143,144] or to instead have conical folded configurations [145].

3.4 Square-Twist Origami. Square-twist origami has fourfold rotational symmetry, with its pattern composed of a central square and four pairs of alternating square and rhombus panels, which was first proposed by Kawasaki and Yoshida [49] when studying crystallographic flat origami. The surrounding square and rhombus panels can be replaced by four pairs of rectangles and trapezoids (Fig. 7(a)), which allows both the unfolded pattern and the folded configuration to be square [85,146,147]. According to the different assignments of mountain and valley creases, there are 16 flat-foldable square-twist patterns [147]. With the consideration of rotational and mirror symmetries, only 4 independent square-twist patterns remain. Crease patterns of the 4 common types of square-twist origami are shown in Fig. 7(a) [146], and their geometry can be parameterized by the two side lengths L and l, and the sector angle ϕ. For easy distinction, the four patterns are named type-1, type-2, type-3, and type-4, from left to right. It has been shown that the type-1 and type-2 are non-rigidly foldable, while the type-3 and type-4 are rigid-foldable [85,148].

For non-rigidly foldable square-twist origami, it was found that the bending DOF of the panel gives rise to an energy barrier which can allow for bistability [2]. By releasing the bending DOF, the elastic energy of the non-rigidly foldable square-twist origami during the folding/unfolding process is mainly from the bending energy of the panels and the folding energy at the creases. To fully understand the bistability mechanism of the non-rigidly foldable square-twist origami, Silverberg et al. [2] studied the mechanical behavior of square-twist origami with type-1 pattern composed of alternating square and rhombus panels under tensile forces by introducing virtual bending creases to capture the panel bending. The unfolding process of the square-twist origami is shown in Fig. 7(b), and variations of the bending energy and the folding energy with respect to the displacement for different sector angles are illustrated in Fig. 7(c). It is seen that there appears to be an energy barrier in the bending energy-displacement curve when the sector angle reaches roughly 20 deg, and the magnitude of the energy barrier increases with the sector angle. In contrast, the folding energy at the creases decreases as the sector angle increases. Therefore, when the sector angle is large enough, the bending energy dominates during the unfolding process, leading to the bistability of the square-twist origami. Also, competition between the bending energy and the folding energy gives rise to a critical sector angle, beyond which the non-rigidly foldable square-twist origami transits from monostable to bistable. Note that this critical sector angle depends on the stiffness ratio of the virtual bending crease and the actual folding crease. Recently, Wang et al. [86] compared the total energy-displacement curve of the type-1 and type-2 square-twist origami for different stiffness ratios of the bending crease and the folding crease. It is shown from Fig. 7(d) that when the stiffness ratio equals 1, the non-rigidly foldable square-twist origami is monostable, while it becomes bistable when the stiffness ratio increases to 5. This indicates that, to achieve the bistability of the non-rigidly foldable square-twist origami, the bending stiffness of the panel should be much larger than the folding stiffness of the crease. By harnessing its

bistability, the non-rigidly foldable square-twist origami has been used for the design of mechanical energy storage devices [149], origami-equivalent compliant mechanisms [150], frequency-reconfigurable origami antennas [151], and mechanical metamaterials with tunable properties [146].

For rigid-foldable square-twist origami, the folding motion can be analyzed using the kinematic method based on the motion transmission path. Figure 7(e) defines the creases and sector angles around the four degree-4 vertices of the square-twist pattern [85]. The creases around the four vertices, i.e., A, B, C, and D, are denoted by a_i, b_i, c_i, and d_i ($i = 1, 2, 3, 4$), respectively. The sector angles of each vertex are represented by α, β, δ, and γ. In type-3 and type-4 patterns, the degree-4 vertices A, B, C, and D form a closed-loop of four spherical 4-revolute (4R) linkages, as shown in Fig. 7(f), whose kinematic motion transmission path can be written as [85]

$$\theta_1^a \to \theta_2^a = \theta_1^b \to \theta_2^b = \theta_1^c \to \theta_2^c = \theta_1^d \to \theta_2^d \to \theta_2^d = \theta_1^a \to \theta_1^a$$

(11)

where $\theta_i^a, \theta_i^b, \theta_i^c$, and θ_i^d are the rotation angles of the joints a_i, b_i, c_i, and d_i, respectively. Equation (11) is the motion compatibility condition of the loop, which must be satisfied for a rigid-foldable square-twist origami. By using the compatibility condition and considering the different assignments of the mountain and valley creases at the vertices, the kinematic equations for type-3 square-twist origami can be written as [85]

$$\tan \frac{\theta_2^a}{2} = \frac{\cos \alpha}{1 - \sin \alpha} \tan \frac{\theta_1^a}{2}, \quad \theta_3^a = -\theta_1^a, \quad \theta_4^a = \theta_2^a$$

$$\theta_1^b = \theta_2^a, \quad \tan \frac{\theta_2^b}{2} = \frac{-\cos \alpha}{1 + \sin \alpha} \tan \frac{\theta_1^b}{2}, \quad \theta_3^b = \theta_1^b, \quad \theta_4^b = -\theta_2^b$$

$$\theta_1^c = \theta_2^b, \quad \tan \frac{\theta_2^c}{2} = \frac{\cos \alpha}{1 - \sin \alpha} \tan \frac{\theta_1^c}{2}, \quad \theta_3^c = -\theta_1^c, \quad \theta_4^c = \theta_2^c$$

$$\theta_1^d = \theta_2^c, \quad \theta_2^d = \theta_1^a, \quad \theta_3^d = \theta_1^d, \quad \theta_4^d = -\theta_2^d$$

(12)
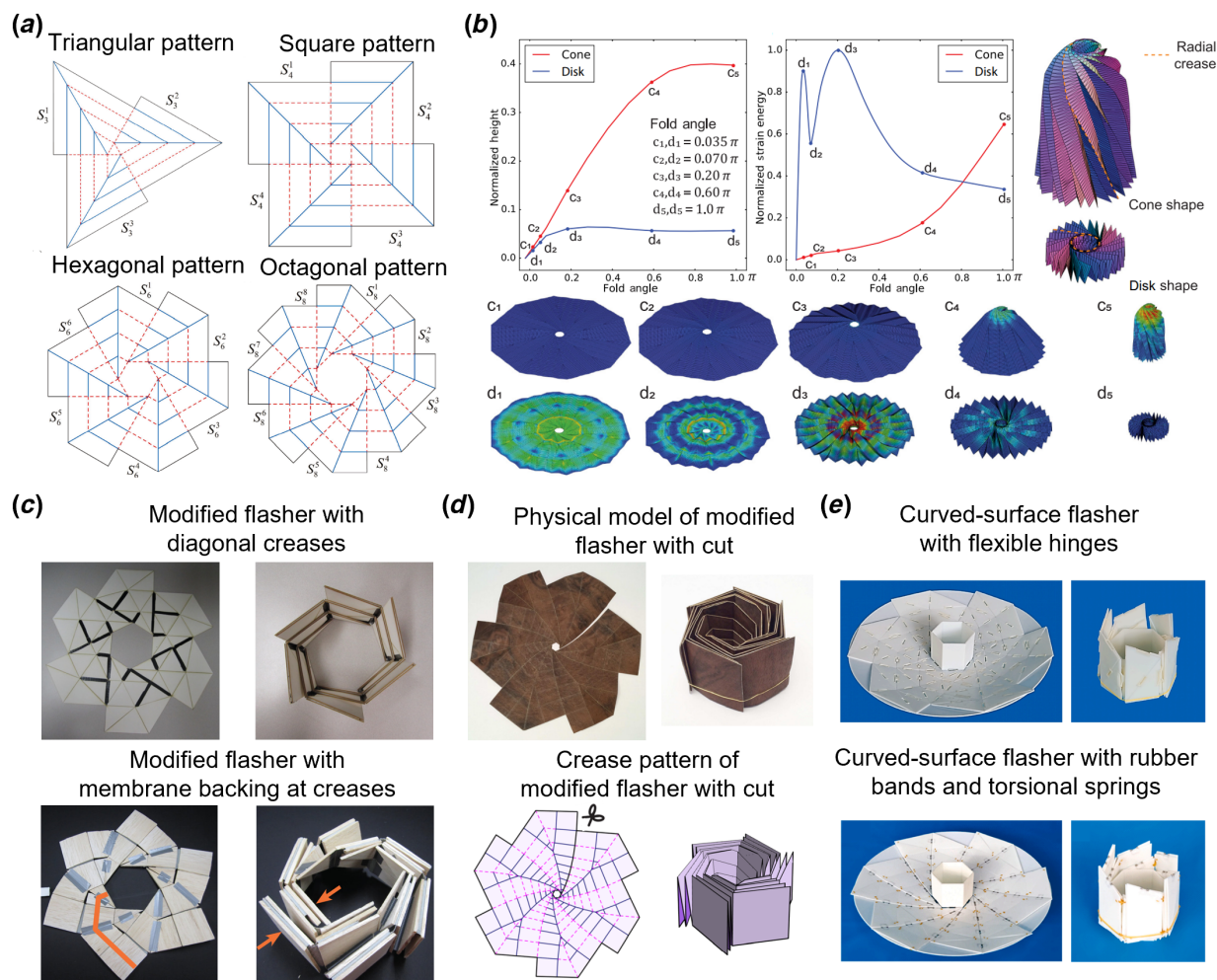
For type-4 square-twist origami, the kinematic equations are given by [85]

$$\tan \frac{\theta_2^a}{2} = \frac{-\cos \alpha}{1 + \sin \alpha} \tan \frac{\theta_1^a}{2}, \quad \theta_3^a = -\theta_1^a, \quad \theta_4^a = \theta_2^a$$

$$\theta_1^b = \theta_2^a, \quad \tan \frac{\theta_2^b}{2} = \frac{\cos \alpha}{1 - \sin \alpha} \tan \frac{\theta_1^b}{2}, \quad \theta_3^b = \theta_1^b, \quad \theta_4^b = -\theta_2^b$$

$$\theta_1^c = \theta_2^b, \quad \tan \frac{\theta_2^c}{2} = \frac{\cos \alpha}{1 - \sin \alpha} \tan \frac{\theta_1^c}{2}, \quad \theta_3^c = -\theta_1^c, \quad \theta_4^c = \theta_2^c$$

$$\theta_1^d = \theta_2^c, \quad \theta_2^d = \theta_1^a, \quad \theta_3^d = \theta_1^d, \quad \theta_4^d = -\theta_2^d$$

(13)

Based on the kinematic equations, the kinematic motion transmission paths for the two types of rigid-foldable square-twist origami are shown in Fig. 7(g) [85]. As can be seen, when given an input rotation angle of one joint, the output rotation angles of the remaining joints can be determined. Therefore, the kinematic motion of the rigid-foldable square-twist origami has only one DOF, which can be further designed into its nonzero-thickness counterpart using the thick-panel origami techniques [152,153].

3.5 Origami Flasher. The origami flasher is a type of rotationally symmetric pattern composed of triangles and trapezoids that form a central polygon, which can be any regular polygon such as the triangular, square, hexagonal, and octagonal flasher patterns [154], as shown in Fig. 8(a). The geometry of the flasher pattern can be determined by three parameters: the side length a and the side number n of the central polygon, and the number of layers m in the radial direction. Note that the side number of the

Fig. 8 Geometric designs and mechanical behaviors of origami flashers. (*a*) Crease patterns of origami flashers with different central polygons. The red dashed lines represent the valley creases, and the blue solid lines denote the mountain creases. (Reproduced with permission from Ref. [154]. Copyright 2022 by Elsevier). (*b*) Variations of the height and strain energy with respect to the folding angle of an origami flasher during the folding to cone or disk shape (Reproduced with permission from Ref. [38]. Copyright 2019, The Authors, published by the American Physical Society). (*c*) Modified origami flasher accommodating for panel thickness with diagonal creases (top) or with membrane backing at creases (bottom) (Reproduced with permission from Ref. [39]. Copyright 2013 by ASME). (*d*) Physical model (top) and crease pattern (bottom) of a single DOF modified flasher with a cut (Reproduced with permission from Ref. [87]. Copyright 2016 by ASME). (*e*) Thick-panel curved-surface origami flasher with flexible hinges (top) or with rubber bands and torsional springs (bottom) (Reproduced with permission from Ref. [154]. Copyright 2022 by Elsevier).

central polygon also determines the rotational symmetry order of the origami flasher. When the panels wrap around the central polygon, the origami flasher can be folded from the flat deployed state to a cylindrical stowed state with a high packing ratio. For example, Zirbel et al. [39] fabricated a physical model of an origami flasher whose deployed-to-stowed diametral ratio is 9.2, and the ratio can be even larger as the number of radial layers increases. This feature makes the origami flasher particularly suitable for space-deployable structures such as solar sails [88], solar arrays [38,39], and deployable antennas [57].

Origami flashers are non-rigidly foldable, which means that they cannot be folded with rigid panels and revolute joints [87,88]. It has been shown that the non-rigid folding of the origami flasher shows a bifurcation behavior [89], and a flat origami flasher can either be folded into a cone shape or a disk shape [38]. Chen et al. [38] studied the height changes and energy landscapes of an origami flasher during the two distinct folding paths, as shown in Fig. 8(*b*). It is seen that the height of the origami flasher during cone-shape folding linearly increases until the radial creases are near vertical, while the height of the origami flasher during disk-shape folding remains unchanged after increasing to
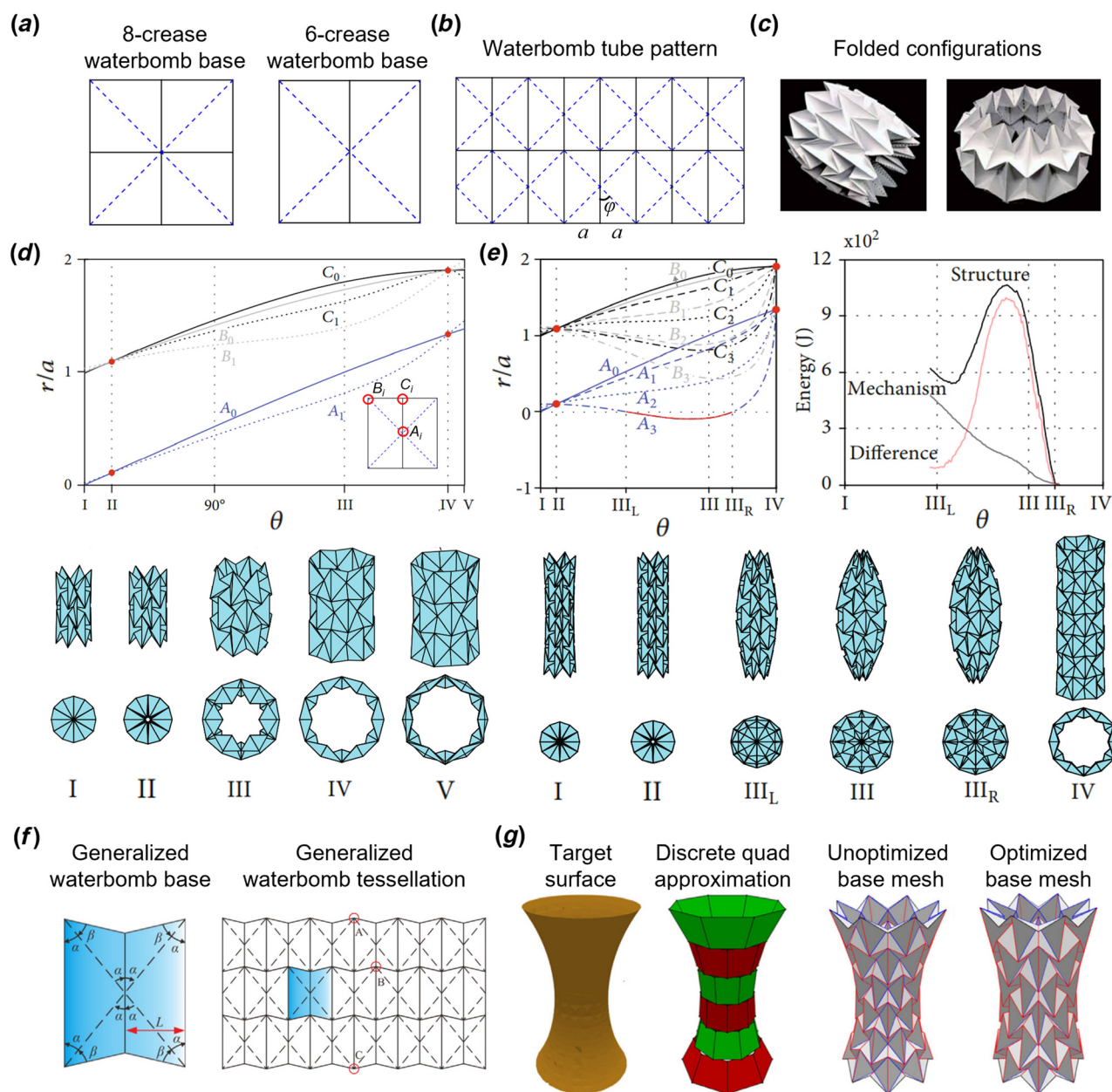
the width of the panels. For the cone-shape folding, the energy landscape monotonically increases. However, for the disk-shape folding, the energy landscape has two energy barriers, and the strain energy in the early stages of folding is much higher than that during the cone-shape folding. Therefore, the origami flasher prefers to fold into the cone shape.

The idealized flasher pattern is zero-thickness, but the thickness of the panels usually cannot be neglected in practical applications. To accommodate the physical thickness of the origami flasher, Zirbel et al. [39] proposed two different methods to modify the pattern design. One method is to allow the quadrilateral panels to fold along their diagonals, which results in the modified flasher pattern consisting of only triangles, as shown in the top row of Fig. 8(*c*). The other method is to apply a membrane backing with specified width at the creases (bottom row of Fig. 8(*c*)), but the gap size to enable rigid-foldability while maximizing the panel surface area needs to be optimized. Both modifications make the flasher pattern rigid-foldable, while both yield origami flashers with multiple DOFs. Lang et al. [87] found that the rigid-foldable origami flasher with a single DOF could be achieved by choosing appropriate sector angles and introducing a cut, as

shown in the top row of Fig. 8(*d*). This modified pattern curves the radial crease lines, and therefore the sector angles are not equal on their two sides (see the bottom row of Fig. 8(*d*)). The origami flasher can also be designed to have a curved-surface configuration in the unfolded state. Several different methods have been developed to achieve such design. For example, Wang et al. [154] projected the planar origami flasher onto the target curved surface to obtain the vertices on the boundary creases and then used numerical methods to obtain the other vertices. After

determining all the vertex positions, the thin-panel curved-surface flasher could be further modified to the thick-panel one by using flexible hinges (top row of Fig. 8(*e*)) or rubber bands and torsional springs (bottom row of Fig. 8(*e*)). Such curved-surface origami flasher can alternatively be realized by removing one wedge of the flasher and connecting the two adjacent wedges of the thickness-accommodating origami flasher [155], or achieved by introducing cuts and tapering the panels in the radial direction [156].

Fig. 9 Geometric design and mechanical behaviors of waterbomb origami. (*a*) Crease patterns of the 8-crease waterbomb base (left) and the 6-crease waterbomb base (right). The dashed lines represent the valley creases, and the solid lines denote the mountain creases. (*b*) Crease pattern of waterbomb tube. (*c*) Folded configurations of waterbomb tube (Reproduced with permission from Ref. [54]. Copyright 2021, The Authors, some rights reserved; exclusive licensee American Association for the Advancement of Science). (*d*) Variations of the radii of vertices in different layers with respect to the folding angle, and unfolding process of a three-layer waterbomb tube with $m = 3$, $n = 6$, and $\varphi = \pi/4$ [165]. (*e*) Variations of the radii of vertices in different layers and strain energy with respect to the folding angle, and unfolding process of a seven-layer waterbomb tube with $m = 7$, $n = 6$, and $\varphi = \pi/4$ (Figures (*d*) and (*e*) are adapted with permission from Ref. [165]. Copyright 2020, The Authors; exclusive Licensee Science and Technology Review Publishing House). (*f*) Crease patterns of the generalized waterbomb base (left) and tessellation (right). The dashed lines represent the valley creases, and the solid lines denote the mountain creases. (Reproduced with permission from Ref. [167]. Copyright 2021 by Elsevier). (*g*) Approximating 3D surfaces of revolution using generalized waterbomb tessellation. (Adapted with permission from Ref. [168]. Copyright 2018 by Oxford University Press).

4 3D-To-3D Origami With Rotational Symmetry

In this section, we introduce the geometric designs and mechanical behaviors of origami with rotational symmetry that can only transform between different 3D configurations, which includes waterbomb origami, modified Miura-ori, Ron Resch origami, and hypar origami. Note that unclosed modified Miura-ori is flat-foldable and rigid-foldable like the standard Miura-ori, however, for a closed modified Miura-ori with rotational symmetry, it is no longer rigid-foldable and flat-foldable due to the closed-loop constraints.

4.1 Waterbomb Origami. Waterbomb origami, also known as origami magic ball, is a well-known rigid-foldable origami with rotational symmetry. The unit cell of waterbomb origami is usually called the waterbomb base, which consists of either four mountain creases and four valley creases (i.e., 8-crease waterbomb base) or two mountain creases and four valley creases (i.e., 6-crease waterbomb base) [48], as shown in Fig. 9(a). The 8-crease waterbomb base is bistable and can snap-fold from the vertex-up state to the vertex-down state under an external actuation [96,157,158], which has been used for the design of mechanical logic devices [159,160]. The 6-crease waterbomb base is much more common, and it can serve as a building block to form a tubular structure with rotational symmetry, i.e., waterbomb tube. The crease pattern of a waterbomb tube composed of repeating 6-crease waterbomb bases is shown in Fig. 9(b), and its geometry can be determined by four parameters: the half-edge length a, the sector angle φ, and the number of the waterbomb bases m and n in longitudinal and circumferential directions, respectively. By folding along the creases and connecting the left and right edges, a waterbomb tube can be obtained. During the folding process, the size of the waterbomb tube in the axial and radial directions changes simultaneously, as shown in Fig. 9(c) [54], allowing for a 3D-to-3D configuration transformation. This feature has been exploited to design various functional structures and devices, such as deployable medical stents [21], vacuum-driven soft grippers [161], peristaltic crawling robots [53,162], and high-load capacity transformable wheels [54].

The rigid folding motion of the waterbomb tube is multi-DOF due to the 6-crease waterbomb base having 3 DOFs [163,164]. When considering the symmetric folding, the overall DOF of the waterbomb tube is reduced to one [48], such that its motion can be described by a single dihedral angle of the waterbomb base. Recently, Ma et al. [165] studied the symmetric folding behaviors of waterbomb tubes with different numbers of units in the longitudinal direction (i.e., layer numbers). Figure 9(d) shows variations of the normalized radii r/a of vertices A_i, B_i, and C_i in different layers with respect to the folding angle θ during the unfolding process of a three-layer ($m = 3$) waterbomb tube consisting of square 6-crease waterbomb bases (i.e., $\varphi = \pi/4$) [165]. The subscript i takes values of 0 and 1 in a three-layer waterbomb tube, corresponding to the waterbomb bases in the middle layer and the top layer, respectively. It is seen from Fig. 9(d) that for a relatively short waterbomb tube, it can be rigidly unfolded from its compactly folded configuration I to the fully expanded configuration V. Particularly, when unfolding to the configuration II and configuration IV, the radii corresponding to the same vertices in different layers are equal (red dots on the curves), which means that the waterbomb tube has a uniform radius. The two special configurations (II and IV) also divide the shapes of the waterbomb tube during folding/unfolding into two categories. Between configurations I and II or configurations IV and V, the radii of the vertices in the middle layer are smaller than those of the top and bottom layers, thus the waterbomb tube has a dog-bone shape. Between configurations II and IV, however, the radii of the vertices in the middle layer are larger than those of the top and bottom layers, giving the waterbomb tube a pineapple shape. This phenomenon is more interesting in a long waterbomb tube, in which the cylindrical surface can become wave-like upon folding [166].

When the waterbomb tube is relatively long, it cannot transform from the compactly folded configuration to the fully deployed configuration through a pure rigid motion. Figure 9(e) illustrates the normalized radii of vertices A_i, B_i, and C_i versus the folding angle θ of a seven-layer ($m = 7$) waterbomb tube [165]. The subscript i takes values of 0, 1, 2, and 3 in a seven-layer waterbomb tube, which corresponds to the waterbomb bases in the middle layer to the top layer in order. Similar to the shorter waterbomb tube, the long waterbomb tube also has two configurations with uniform radius (configurations II and IV), between which the folded configuration of the waterbomb tube has a pineapple shape. However, there exist two critical configurations, III_L and III_R, of the long waterbomb tube between the two uniform radius configurations. At these two critical configurations, the radius of the vertex A_3 (at the top layer) equals zero, which means that the waterbomb bases at the two ends of the tube are closed. Rigid motion between the two critical configurations leads to a negative radius of the vertex at the top layer (see the red curve segment in Fig. 9(e)), revealing that the waterbomb tube is non-rigidly foldable within this range and that the transition between the two critical states requires structural deformation. To evaluate the effect of structural deformation between configurations III_L and III_R, Fig. 9(e) further compares the elastic energy of the waterbomb tube when it is modeled as a mechanism or as a deformable structure. In the mechanism analysis, panels are allowed to freely penetrate each other and only the strain energy stored in the creases is considered. In the structural analysis, the elastic energy from both the panels and the creases is considered using the finite element method. The difference between the two energies from the mechanism and structural analyses represents the elastic energy due to panel deformations. It is seen that panel deformations contribute most of the elastic energy during the unfolding process and give rise to two energy minima for the energy landscape, which means that the waterbomb tube has two stable states during the transition between configurations III_L and III_R.

The generalized waterbomb base consisting of two isosceles trapezoids can also be tessellated to form a tubular structure with rotational symmetry. As shown in Fig. 9(f), the geometry of the generalized waterbomb base is characterized by three parameters: the two sector angles α and β, and the half-width L [167]. When $\alpha + \beta = \pi/2$, the generalized waterbomb base degenerates to the rectangular counterpart. The generalized waterbomb tessellation has an enlarged design space, which can be used to inversely design 3D structures with rotational symmetry [168–170]. Zhao et al. [168] made the first attempt to use the generalized waterbomb tessellation to approximate 3D surfaces of revolution. As shown in Fig. 9(g), the target surface is first discretized into a quadrilateral approximation, and then an unoptimized base mesh is generated by creating generalized waterbomb bases in each quadrilateral panel. Finally, optimization of the base mesh results in a developable waterbomb tessellation. In the optimization, the six sector angles around an interior vertex should sum to 2π to satisfy the developability constraint. By using this method, various rotationally symmetric structures that approximate a target surface of revolution can be obtained.

4.2 Modified Miura Origami. In addition to the cylindrical Miura-ori discussed in Sec. 3.3, there are two other modified Miura-ori patterns that can be used to design 3D structures with rotational symmetry, while not being able to fold to 2D configurations. One is the generalized Miura-ori, also known as quadrilateral mesh origami, which is the most general form of the famed Miura-ori, and was first proposed by Tachi [72]. Unlike the standard Miura-ori cell containing four congruent parallelograms with a degree-4 vertex, the generalized Miura-ori cell is composed of free-form quadrilaterals with different edge lengths and sector angles, as shown in Fig. 10(a) [90]. To preserve the developability and flat-foldability of the standard Miura-ori, the sector angle α_i
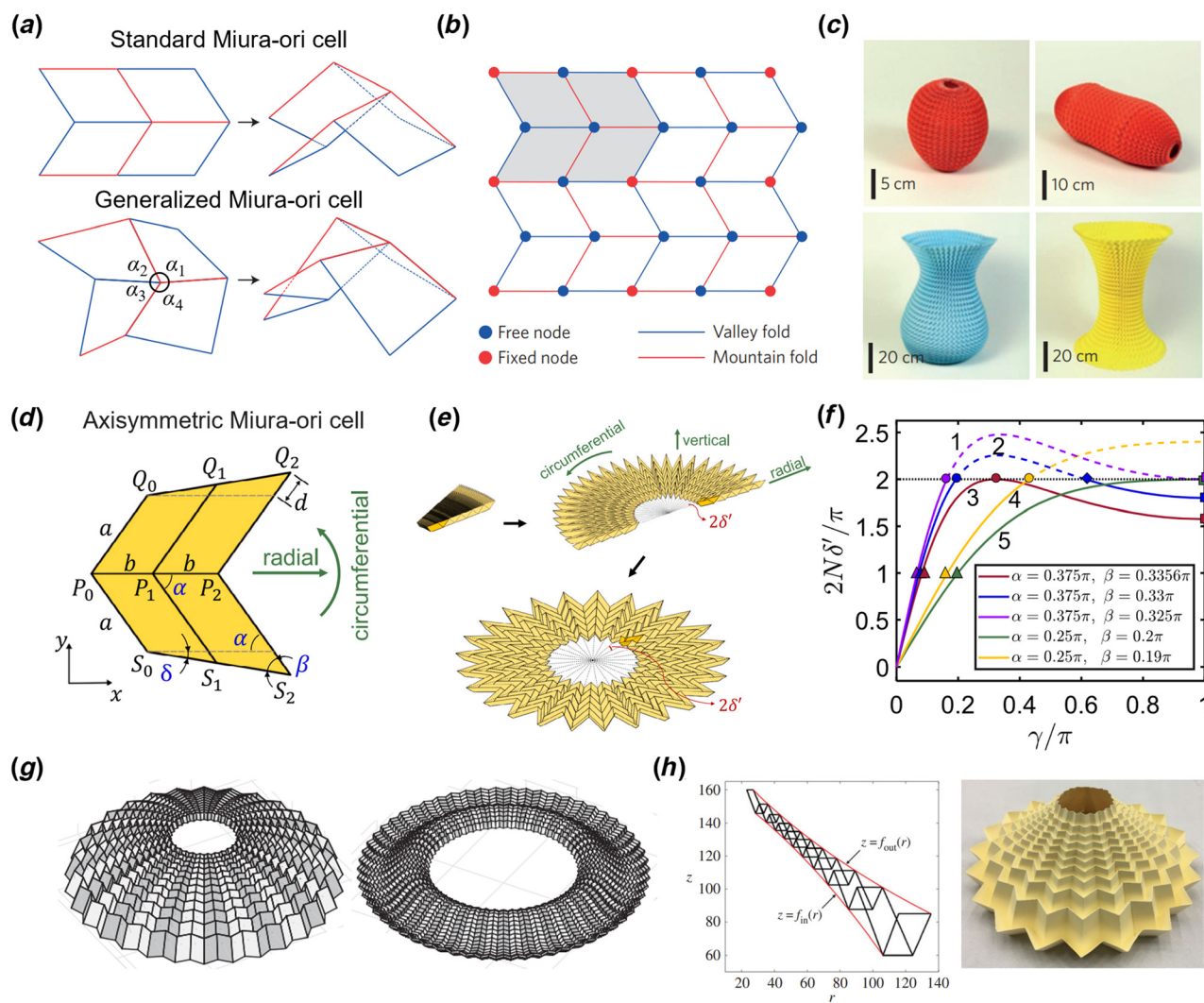
($i = 1, 2, 3, 4$) around the degree-4 vertex of the generalized Miura-ori needs to satisfy [72,90]

$$\sum_{i=1}^{4} \alpha_i = 2\pi \qquad (14)$$

$$\alpha_1 + \alpha_3 = \alpha_2 + \alpha_4 = \pi \qquad (15)$$

The generalized Miura-ori is commonly used for the inverse design of deployable structures with target geometric shapes, due to its flexible design space. Based on the generalized Miura-ori, Dudte et al. [90] developed a constrained optimization method to design Miura-ori tessellations that approximate target 3D curved surfaces. The target curved surface is first discretized into a Miura-ori-like tessellation as an initial guess for the optimization, as shown in Fig. 10(b), in which the four corner nodes of each

unit cell are fixed at the target surface such that the initial guess is close to the target surface, and the remaining edge nodes and central nodes are varied to find the optimal solutions. Then, planarity, developability, and flat-foldability constraints are enforced, and the node positions are optimized to minimize the changes in the lengths of pattern edges and cross edges of the initial guess. By utilizing this method, the optimized generalized Miura-ori tessellation can approximate surfaces of revolution with various Gaussian curvatures, such as the demonstrations shown in Fig. 10(c), which have positive curvature (upper left), positive mixed with zero curvature (upper right), positive mixed with negative curvature (lower left), and negative mixed with zero curvature (lower right). However, these doubly curved Miura-ori tessellations are not flat-foldable and rigid-foldable, as the flat-foldability condition (Eq. (15)) in the algorithm cannot be exactly satisfied, which means that they cannot be folded into 2D configurations. To achieve the flat-foldable and rigid-foldable design of generalized

Fig. 10 Design of modified Miura-ori tessellations with rotational symmetry. (a) Schematics of standard and generalized Miura-ori cells [90]. The blue lines represent the valley creases, and the red lines denote the mountain creases. (b) Initial guess of the generalized Miura-ori tessellation with fixed and free nodes for the numerical optimization method [90]. (c) Generalized Miura-ori tessellations that approximate surfaces of revolution with various Gaussian curvatures (Figures (a)–(c) are adapted with permission from Ref. [90]. Copyright 2016 by Springer Nature). (d) Schematic of an axisymmetric Miura-ori cell [91]. P_0P_1, P_1S_1, and P_1Q_1 are the valley creases, and P_1P_2 is the mountain crease. (e) Folding process of an AMO tessellation [91]. (f) Variation of the central angle with respect to the deploying parameter. Dashed parts of lines 1 and 2 denote the non-rigidly foldable region (Figures (d)–(f) are adapted with permission from Ref. [91]. Copyright 2022 by Elsevier). (g) AMO tessellations approximating surfaces of revolution with quadratic (left) or sinusoidal (right) profiles (Adapted with permission from Ref. [173]. Copyright 2019 by ASME). (h) AMO tessellation simultaneously approximating a target inner surface with positive Gaussian curvature and a target outer surface with negative Gaussian curvature (Reproduced with permission from [73]. Copyright 2017, The Authors, published by the Royal Society).
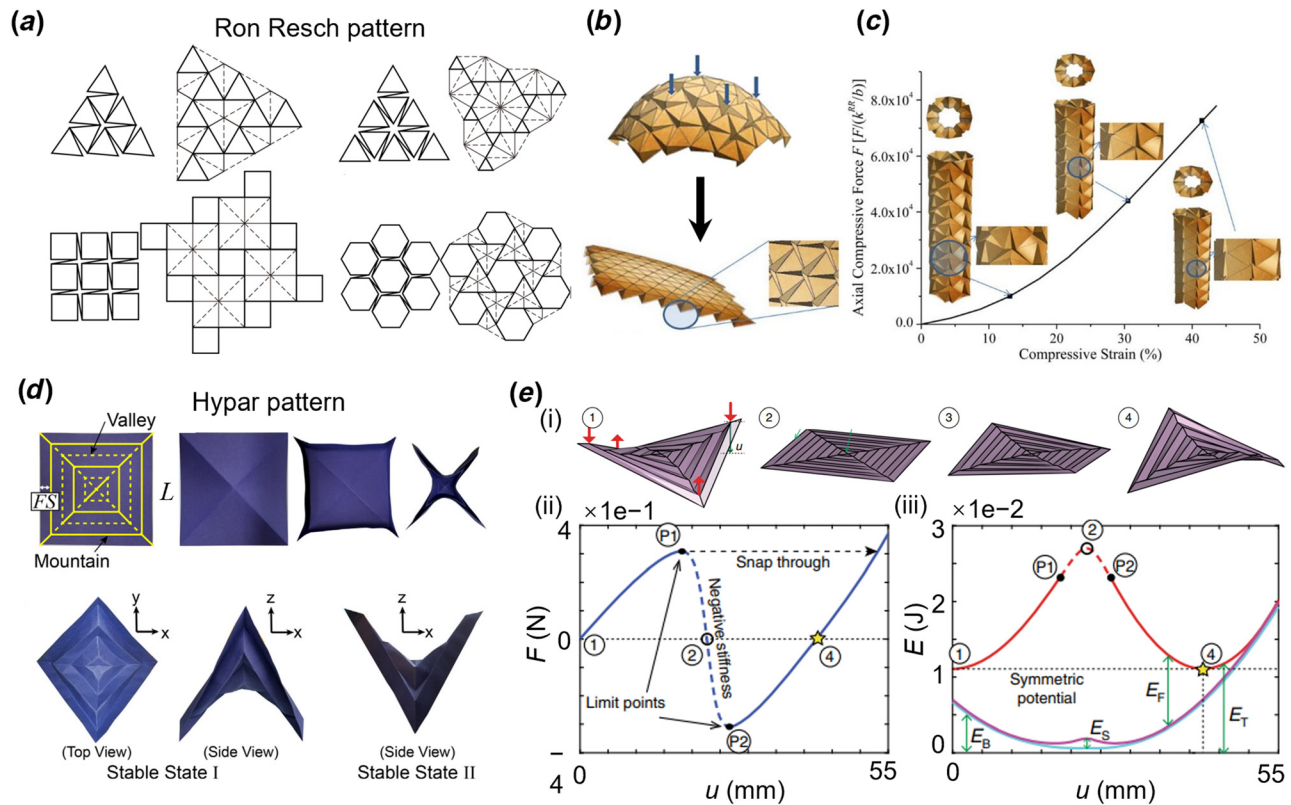
Miura-ori tessellations, several improved constraint optimization algorithms have been developed [92,171,172], but they are limited to approximating unclosed curved surfaces.

The other modified Miura-ori pattern that can achieve rotationally symmetric structural designs is the axisymmetric Miura-ori (AMO) [73,91,173]. As shown in Fig. 10(d), a representative AMO cell contains four trapezoids symmetrical about the collinear crease, and its geometry can be characterized by the circumferential edge length a, the radial edge length b, the major sector angle α, and the minor sector angle β, where $0<\beta<\alpha<\pi/2$ [91]. The distinction of an AMO cell from the standard Miura-ori cell can be described by a deviation angle δ, where $\delta = \alpha - \beta$. When $\delta = 0$, the AMO cell degenerates to the standard Miura-ori cell. Also, δ equals half of the central angle of the AMO cell. To form an AMO tessellation with rotational symmetry, the AMO cells are replicated in the circumferential direction, while the circumferential edge lengths of the AMO cells in the radial direction are iteratively enlarged to be compatible with the adjacent cells. As shown in Fig. 10(e), the AMO tessellation can be deployed from a compact folded state to a partially folded state, and finally form a closed-loop configuration [91]. By introducing the vertical projection δ' of the deviation angle δ, the angular motion of the AMO tessellation is characterized by [91]

$$\tan \delta' = \frac{(t_{\alpha\beta} - 1)\tan \alpha \sin(\gamma/2)}{t_{\alpha\beta} + \tan^2\alpha \sin^2(\gamma/2)} \quad (16)$$

where the parameter $t_{\alpha\beta} = \tan\alpha/\tan\beta$, and γ is the deploying parameter. Figure 10(f) shows the variation of the central angle $2N\delta'$ with respect to the deploying parameter γ for an AMO tessellation with N cells [91]. Note that when $2N\delta'$ reaches 2π, the AMO tessellation is closed. It is seen that with appropriate sector angles α and β, the AMO tessellation can have one closed state or two closed states. For the former case, the AMO tessellation at the closed state either gets locked (lines 4 and 5) or continues deploying to an unclosed developable state (line 3). For the latter case, the AMO tessellation at both closed states gets locked (lines 1 and 2), and transition between the two closed states cannot be achieved without panel deformation.

When the unit cells in different layers have the same radial edge lengths, the AMO tessellation remains in-plane during folding/unfolding. By varying the radial edge lengths of the unit cells in different layers, the AMO tessellation forms a doubly curved folded configuration whose shape can be inversely designed to approximate a target surface of revolution. Due to the rotational symmetry, target designs can easily be achieved by minimizing the distance between the vertices of a strip extracted from the tessellation and the generatrix of the target surface. Using this method, the doubly curved AMO tessellation can approximate not only a single target surface, such as a surface of revolution with quadratic profile (left side of Fig. 10(g)) or sinusoidal profile (right side of Fig. 10(g)) [173], but can also approximate two target surfaces simultaneously. This is demonstrated in Fig. 10(h), in which the target inner surface has positive Gaussian curvature while the target outer surface has negative Gaussian curvature

Fig. 11 Geometric designs and mechanical behaviors of Ron Resch origami and hypar origami. (a) Basic triangular pattern with degree-6 vertices (upper left), triangular pattern with degree-12 vertices (upper right), square pattern with degree-8 vertices (lower left), and hexagonal pattern with degree-6 vertices (lower right) of Ron Resch origami. The dashed lines represent the valley creases, and the solid lines denote the mountain creases. (Reproduced with permission from Ref. [174]. Copyright 2013 by ASME). (b) Dome-like and plate-like folded configurations of Ron Resch origami [14]. (c) Force-strain curve of Ron Resch tube (Figures (b) and (c) are adapted with permission from Ref. [14]. Copyright 2014, The Authors, published by Springer Nature). (d) Crease pattern and folded configurations of hypar origami (Reproduced with permission from Ref. [93]. Copyright 2018 by Elsevier). (e) Snap-folding process (i), force–displacement curve (ii), and energy landscape (iii) of hypar origami (Adapted with permission from Ref. [5]. Copyright 2019, The Authors, published by Springer Nature).

[73]. Note that these AMO tessellations can only be flat-foldable and rigid-foldable when they are unclosed.

4.3 Ron Resch Origami. Ron Resch origami was originally proposed by Ronald Dale Resch, who was inspired by paper crimping in the 1960s [74]. As shown in the upper left of Fig. 11(*a*), a traditional Ron Resch pattern is composed of equilateral and right triangles, and every patch of six adjacent right triangles forms a large equilateral triangle with a degree-6 vertex. Tachi [174] found that the basic Ron Resch pattern could be generated by the insertion of a star-like folded tuck, and using this method he proposed another three types of Ron Resch patterns, i.e., the triangular pattern with degree-12 vertices (upper right of Fig. 11(*a*)), the square pattern with degree-8 vertices (lower left of Fig. 11(*a*)), and the hexagonal pattern with degree-6 vertices (lower right of Fig. 11(*a*)). Ron Resch origami is rigid-foldable but with multiple DOFs [174,175], and it can be folded into a dome-like configuration with rotational symmetry. When subjected to compressive forces, the Ron Resch dome can finally transform into a sandwich plate (i.e., the Ron Resch plate), as shown in Fig. 11(*b*). Lv et al. [14] reported that a Ron Resch paper plate with actual mass of 4.55 grams can carry a 32.4-pound load. Thus, the Ron Resch plate has a remarkable load-bearing capability, which has been utilized for the design of energy absorption structures [176,177]. The Ron Resch pattern can also be rolled up to form a tube with rotational symmetry. Figure 11(*c*) shows the force–strain curve of a Ron Resch tube under an axial compressive force [14]. As the compressive strain increases, the tube gradually shortens its length and reduces its radius, showing a negative Poisson's ratio characteristic. When the strain increases to about 45%, the tube reaches the completely folded state without buckling, indicating that the Ron Resch tube also has a good load-bearing capability.

4.4 Hypar Origami. The hypar pattern is composed of concentric squares and diagonals with alternating mountain and valley creases, as shown in Fig. 11(*d*) [93], which can be folded into a pleated hyperbolic paraboloid with nonzero Gaussian curvature [178]. The more concentric squares one folds, the closer the folded configuration is to a true hyperbolic paraboloid [75]. The geometry of the hypar pattern is determined by two parameters: the edge length of the outermost square L and the number of concentric layers n. The hypar origami is not rigid-foldable, which means that it cannot fold without panel deformation [179]. Interplay between the panel deformation and crease folds enables two stable states for the hypar origami [93]. In particular, the two stable states are symmetric to each other and their folding angles of creases are the same, while the twisting directions of the panels are reversed. When subjected to a pair of vertical forces at opposite corners (see Fig. 11(*e*-i)), the hypar origami snap-folds from one stable configuration to the other, accompanied by a negative-stiffness stage [5], as shown in Fig. 11(*e*-ii). During the snap-folding process, bending energy of the panels and folding energy at the creases dominate during folding, while stretching energy of the panels contributes little to the total elastic energy (see Fig. 11(*e*-iii)). The resulting energy landscape has two equal energy minima, corresponding to the two stable states. Therefore, the energy barrier of hypar origami is also symmetric. By utilizing its bistability, hypar origami has enabled the design of antennas with reconfigurable polarization [180] and programmable multistable metasurfaces [5,181].

5 2D-To-2D Origami With Rotational Symmetry

Classical origami with rotational symmetry usually has a 3D configuration and can only be folded into a 2D flat-folded state or another 3D state. Here, we introduce two types of foldable truss structures with rotational symmetry, i.e., scissor trusses and ring origami, which can be considered origami without panels. Note that, based on different structural designs, these two foldable structures can achieve not only 2D to 2D configuration transformation, but also 3D to 2D and 3D to 3D configuration transformations.

5.1 Scissor Trusses. Scissor trusses are created by interconnecting multiple scissor units at their end points, and they can change their shape from a compact stowed state to an expanded functional state. Due to their light weight, mobility, and impressive packing ability, scissor trusses have widespread applications ranging from architecture and engineering to aerospace [67,182–184]. The concept of scissor trusses was first proposed in 1961 by Pinero [185], a Spanish architect who used simple scissor units to design a reticular mobile theater. A scissor unit is composed of a pair of bars connected with a revolute joint. The revolute joint, also known as the scissor hinge, allows the scissor unit to rotate about an axis normal to the unit plane. Scissor units can be classified into three categories: translational scissor units, polar scissor units, and angulated scissor units [66,186]. Based on the different types of scissor units, various 2D and 3D deployable structures with rotational symmetry can be designed.

Translational scissor units and polar scissor units both consist of two straight bars. As shown in Fig. 12(*a*), when the unit lines (dashed lines) connecting the upper and lower ends of the two bars are parallel, the scissor unit is a translational unit [95]. Otherwise, the unit lines intersect at one point, which characterizes a polar scissor unit [187], as illustrated in Fig. 12(*b*). The geometry of the general translational unit can be described by four parameters: three size parameters l_1, l_2, and k, and one deployment angle ϕ. To ensure that the unit lines are always parallel, the length ratio k is the same for two segments of each bar. When $k=1$ and $l_1=l_2$, the basic translational scissor unit is obtained, which contains two identical straight bars with the hinge located at the midpoints of the two bars. Translational scissor units can be tessellated in different manners to construct diverse planar or spatial deployable truss structures with rotational symmetry. By tessellating the basic translational units in two perpendicular directions, one can obtain planar scissor trusses that can be folded from their deployed 2D planar states to stowed 3D cylindrical states, such as the ring and the square scissor trusses [95,184] shown in Fig. 12(*c*). By connecting multiple closed-loop modules consisting of translational scissor units along one direction, retractable towers can be obtained [184], as illustrated in Fig. 12(*d*). With general translational scissor units as the building blocks, 3D trusses with curved surfaces can be designed, such as the conical scissor truss and the pyramid scissor truss [95] presented in Fig. 12(*e*).

For the polar scissor unit, the geometry of its general form is dependent on five parameters: four size parameters l_1, l_2, k_1, and k_2, and one deployment angle ϕ [188]. During the deployment, the segment angle α between the unit lines varies with the deployment angle. When $l_1=l_2$ and $k_1=k_2$, the general polar unit reduces to the basic polar unit, which has two identical straight bars with the hinge located away from their midpoints. Like translational units, polar units can also be used to design deployable structures with rotational symmetry, such as the scissor double-ring truss (Fig. 12(*f*)) [189,190] and the spherical scissor truss (Fig. 12(*g*)) [191,192] built from basic polar units, and the parabolic scissor truss (Fig. 12(*h*)) [193] constructed from general polar units.

Unlike translational and polar units which have straight bars, angulated scissor units are composed of two angulated bars with characteristic kink angles and were invented by Hoberman in the 1990s [194,195]. The unit lines of the angulated scissor unit intersect at a single point, and the resulting segment angle between the unit lines remains constant during the deployment [94,196]. Hoberman's angulated scissor unit consists of two identical angulated bars with equal semi-lengths and kink angles, as shown in Fig. 13(*a*). Its geometry can be captured by three parameters: the semi-bar length l, the kink angle ϕ, and the deployment angle θ. During the deployment, the segment angle α is independent of the deployment angle, and $\alpha = \pi - \phi$ [94]. Later on, You and

Pellegrino [94] proposed two types of generalized angulated units. For the type-1 angulated unit (Fig. 13(b)), the two angulated bars have equal semi-lengths but different kink angles ϕ and ψ. In this case, the segment angle $\alpha = \pi - (\psi + \phi)/2$. For the type-2 angulated unit (Fig. 13(c)), the two angulated bars have proportional semi-lengths but equal kink angles ϕ, and the segment angle $\alpha = \pi - \phi$. Benefitting from its constant segment angle, angulated scissor units can be used to design radially deployable closed-loop structures [182,197,198]. By tessellating the angulated scissor units in the circumferential direction, planar deployable ring truss structures enabling 2D to 2D configuration transformation can be obtained, such as the circular ring truss (Fig. 13(d)) [38,199], the octagonal ring truss (Fig. 13(e)) [94], and the inner layer retractable octagonal ring truss (Fig. 13(f)) [94]. By tessellating angulated scissor units in more directions, radially deployable spherical structures with 3D to 3D configuration transformations, such as the well-known Hoberman sphere (Fig. 13(g)) [194,197] and Iris dome [195], or axisymmetric 3D structures like the half-ellipsoidal truss (Fig. 13(h)) and the hyperboloid truss (Fig. 13(i)) [200] can be constructed.

5.2 Ring Origami.
Ring origami is a class of foldable structures of different geometries formed by closed-loop rods. In the past decades, attention was only focused on the circular ring, which can be folded to a configuration of three overlapping loops with radius of only one-third of the initial radius [70,201,202]. The circular ring can therefore reduce to only 11.1% of its initial size upon folding, which can be used for the design of deployable functional structures [203–205]. With this unique packing ability in mind, Wu et al. [68,69] recently generalized the ring origami design to various polygons. Their numerical and experimental results show that rounded-corner polygonal rings made of rods with rectangular cross section can also be folded to small-volume configurations similar to the circular ring, while the height-to-thickness ratio of the cross section is critical to rings' foldability. Table 2 presents the initial and folded geometric configurations and packing ratios (ratio of folded area to initial area) of various ring origami. It is seen that all of these rings have 2D configurations in both the initial and folded states, undergoing 2D to 2D configuration transformations upon folding. Moreover, the multiple loops of the folded states of the triangular, square, pentagonal,
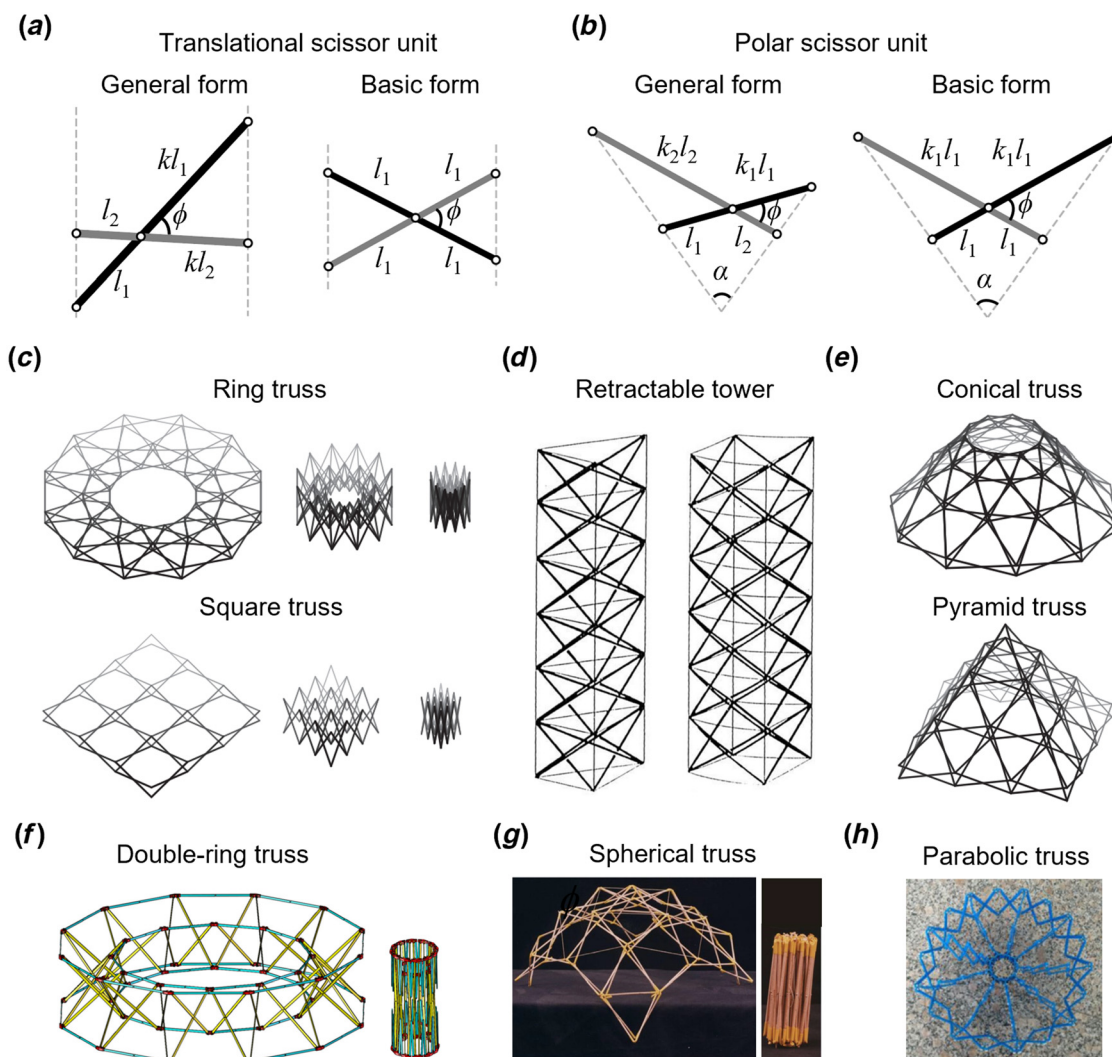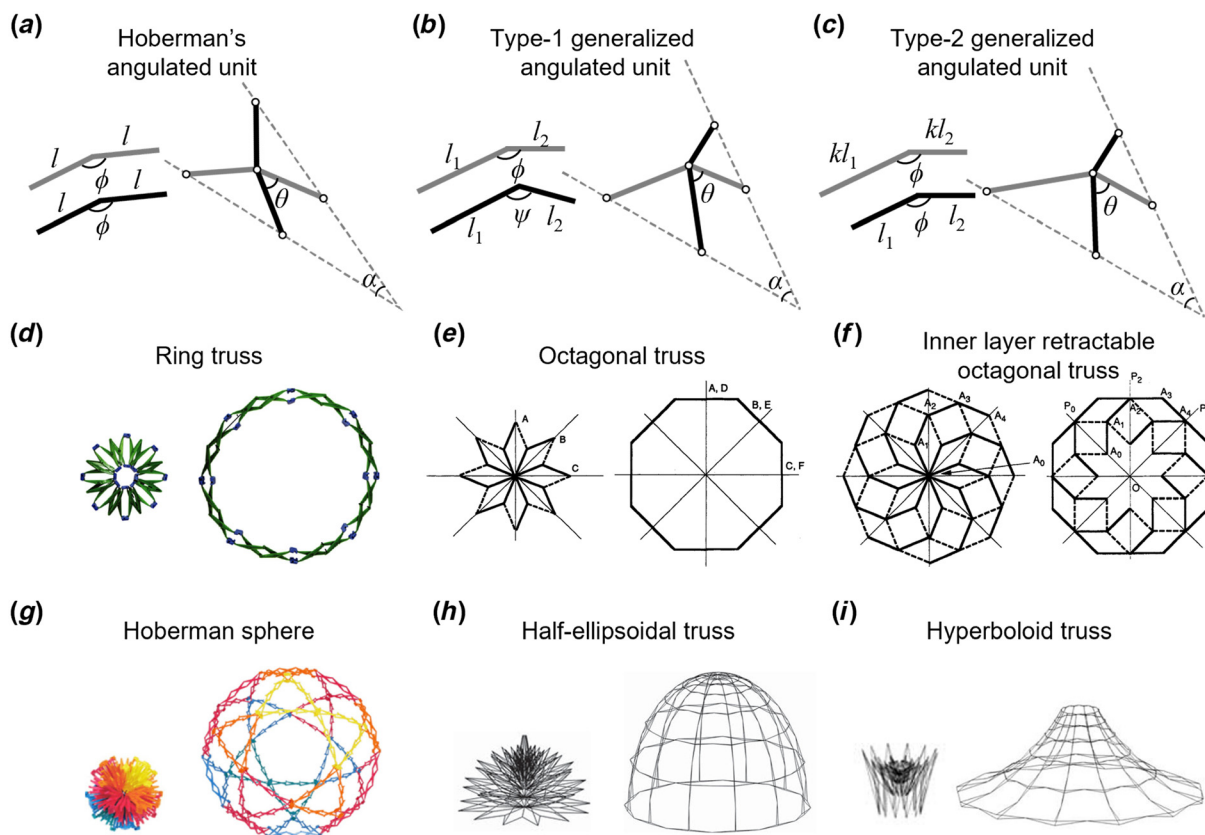

Fig. 12 Scissor trusses made of translational units and polar units. (*a*) Schematics of general and basic translational scissor units. (*b*) Schematics of general and basic polar scissor units. (*c*) Expandable ring scissor truss and square scissor truss [95]. (*d*) Retractable towers with triangular cross section and square cross section (Reproduced with permission from Ref. [184]. Copyright 1993 by SAGE Publications). (*e*) Conical scissor truss and pyramid scissor truss (Figures (*c*) and (*e*) are reproduced with permission from Ref. [95]. Copyright 2017 by Elsevier). (*f*) Scissor double-ring truss (Reproduced with permission from Ref. [189]. Copyright 2019 by Elsevier). (*g*) Spherical scissor truss (Adapted with permission from Ref. [191]. Copyright 2021 by Elsevier). (*h*) Parabolic scissor truss (Reproduced with permission from Ref. [193]. Copyright 2020, The Authors, published by Springer Nature).

Fig. 13 Scissor trusses made of angulated units. (*a*) Schematic of Hoberman's angulated unit. (*b*) Schematic of type-1 generalized angulated unit. (*c*) Schematic of type-2 generalized angulated unit. (*d*) Radially expandable ring truss (Adapted with permission from Ref. [38]. Copyright 2019, The Authors, published by the American Physical Society). (*e*) Radially expandable octagonal truss [94]. (*f*) Inner layer retractable octagonal truss (Figures (*e*) and (*f*) are reproduced with permission from Ref. [94]. Copyright 1997 by Elsevier). (*g*) Hoberman sphere (Reproduced with permission from Ref. [197]. Copyright 2007 by Elsevier). (*h*) Half-ellipsoidal truss [200]. (*i*) Hyperboloid truss (Figures (*h*) and (*i*) are reproduced with permission from Ref. [200]. Copyright 2020 by American Society of Civil Engineers).

Table 2 Geometric configurations and packing ratios of various ring origami

Geometry	Triangle	Square	Pentagon	Hexagon	Heptagon	Octagon
Initial state						
Folded state						
Packing ratio	33.0%	25.0%	18.7%	10.6%	14.3%	13.2%

Geometry	Nonagon	Decagon	Hendecagon	Dodecagon	Circle
Initial state					
Folded state					
Packing ratio	10.8%	12.4%	12.3%	10.8%	11.1%

heptagonal, octagonal, decagonal, and hendecagonal rings are not fully overlapping, thus their packing ratios are larger than that of the circular ring. To achieve an efficient packing, the polygonal ring needs to have an edge number of $3n$ ($n \geq 2$), such that it can be folded into a three-loop, fully overlapping configuration. For instance, the hexagonal, nonagonal, and dodecagonal rings, whose packing ratios are only 10.6%, 10.8%, and 10.8% of their initial configurations, respectively, have even greater packing abilities than the circular ring.

Ring origami with rationally designed geometric parameters can snap-fold in a self-guided manner when mechanical instability of the rod is triggered through application of either twisting or bending loads to the ring. To fully understand the snap-folding mechanism of ring origami, Sun et al. [206] developed a unified theoretical framework for various ring origami based on the Kirchhoff rod model. The governing equations for the rod model can be written as

$$
\begin{aligned}
&F_1' = F_2 k_3 - F_3 k_2, \quad F_2' = F_3 k_1 - F_1 k_3, \quad F_3' = F_1 k_2 - F_2 k_1 \\
&k_1' = k_1^{(u)\prime} + \frac{1}{\alpha} F_2 + \left(\frac{\beta}{\alpha} - \frac{1}{\alpha} \right) k_2 k_3 \\
&k_2' = -\frac{1}{\beta} F_1 - \left(\frac{\alpha}{\beta} - \frac{1}{\beta} \right) k_1 k_3 + \frac{\alpha}{\beta} k_1^{(u)} k_3 \\
&k_3' = (\alpha - \beta) k_1 k_2 - \alpha k_1^{(u)} k_2 \\
&q_0' = \frac{1}{2}(-q_1 k_1 - q_2 k_2 - q_3 k_3), \quad q_1' = \frac{1}{2}(q_0 k_1 - q_3 k_2 + q_2 k_3) \\
&q_2' = \frac{1}{2}(q_3 k_1 + q_0 k_2 - q_1 k_3), \quad q_3' = \frac{1}{2}(-q_2 k_1 + q_1 k_2 + q_0 k_3) \\
&r_1' = 2(q_1 q_3 + q_0 q_2), \quad r_2' = 2(q_2 q_3 - q_0 q_1), \quad r_3' = 2\left(q_0^2 + q_3^2 - \frac{1}{2} \right)
\end{aligned}
$$

$$(17)$$

where (F_1, F_2, F_3) and (k_1, k_2, k_3) are components of the resultant force $\mathbf{F}$ and the Darboux vector $\mathbf{k}$ in the local director basis ($\mathbf{d}_1$, $\mathbf{d}_2$, $\mathbf{d}_3$), respectively. (r_1, r_2, r_3) are components of the position vector $\mathbf{r}$ in the global director basis ($\mathbf{E}_1$, $\mathbf{E}_2$, $\mathbf{E}_3$), and (q_0, q_1, q_2, q_3) are components of a unit quaternion $\mathbf{q}$ used for relating the local basis to the global basis, whose inner product $|\mathbf{q}| = q_0^2 + q_1^2 + q_2^2 + q_3^2 = 1$. Note that all these variables (F_i, k_i, r_i, q_0, q_i) ($i = 1, 2, 3$) are functions of the arc length coordinate s, and $(\bullet)'$ denotes differentiation with respect to the arc length s. Moreover, the parameters α and β are dimensionless bending-to-torsional rigidity ratios of the cross section, and $k_1^{(u)}$ is the in-plane natural curvature of the rod in the unstressed state.

It is seen from Eq. (17) that there are 13 first-order ordinary differential equations for the Kirchhoff rod model, which involves 13 unknown variables, leading to a well-posed two-point boundary value problem (BVP) when equipped with appropriate boundary conditions. For a circular ring with continuous natural curvature, the above rod model can be directly used to study the folding behavior under different loading methods. However, for a polygonal ring, the natural curvatures are discontinuous at the joints of the straight edges and the rounded corners. In this case, the ring needs to be divided into multiple segments with each segment being modeled as a Kirchhoff rod. If the 13 variables in the Kirchhoff rod model are arranged into a vector $\mathbf{u}$, i.e.

$$\mathbf{u} = (F_1, F_2, F_3, k_1, k_2, k_3, r_1, r_2, r_3, q_0, q_1, q_2, q_3) \quad (18)$$

the governing equations in Eq. (17) can be denoted as

$$\mathbf{u}' = \mathbf{g}(\mathbf{u}, k_1^{(u)}, \alpha, \beta) \quad (19)$$

where $\mathbf{g}$ is a function representing the relation between $\mathbf{u}'$ and $\mathbf{u}$. For a polygonal ring composed of n segments, the governing equations can be augmented as follows,

$$
\begin{aligned}
\frac{d}{d\underline{s}} \left(\mathbf{u}^{(1)}, \mathbf{u}^{(2)}, \ldots, \mathbf{u}^{(n)} \right) = &\left[\frac{L_0^{(1)}}{L} \mathbf{g}\left(\mathbf{u}^{(1)}, k_1^{(u)(1)} \right), \right. \\
&\left. \frac{L_0^{(2)}}{L} \mathbf{g}\left(\mathbf{u}^{(2)}, k_1^{(u)(2)} \right), \ldots, \frac{L_0^{(n)}}{L} \mathbf{g}\left(\mathbf{u}^{(n)}, k_1^{(u)(n)} \right) \right]
\end{aligned}
$$

$$(20)$$

where $\underline{s} \in [0, 1]$ is a unified arc length for all different segments, $L_0^{(i)}$ is the length of the ith ($i = 1, 2, \cdots, n$) segment, and L is an identical reference length. After augmentation, the polygonal ring with n segments has $13n$ governing equations containing $13n$ unknown variables, which requires $13n$ boundary conditions to produce a well-posed two-point BVP. The well-posed BVP system can be solved using various numerical continuation methods.

Taking the hexagonal ring as an example, snap-folding behaviors of hexagonal rings under different loading methods using the multi-segment rod model are studied in Fig. 14. A schematic of a hexagonal ring with edge length a, corner radius r, cross section height h, and cross section thickness t, subjected to a pair of twisting moments (blue arrows) at corners or a pair of bending moments (orange arrows) at the middle of edges is shown in Fig. 14(a). Theoretical predictions of the normalized moment versus twisting angle and bending angle curves are presented in Figs. 14(b) and 14(c), respectively. Note that for a foldable ring, the moment tends to decrease to zero when approaching the final state, while the moment continues to increase in the latter folding stages of an unfoldable ring. It is seen that, for the two loading methods, the hexagonal ring with $h/t = 1$ is always unfoldable. However, the hexagonal ring with $h/t = 2$ or 5 becomes foldable, indicating that a foldable ring should have a relatively large height-to-thickness ratio of its cross section. In particular, the ring with $h/t = 5$ under twisting loads experiences a snap-back instability during the folding process, while only snap-through instability is observed for the other foldable cases. Moreover, the stability of the folded configuration of the ring can be determined by the slope of the moment-twisting angle (or bending angle) curve at the final state. A negative slope means that the folded state is unstable and that the removal of the external loading would cause the ring to deploy. Conversely, a positive slope implies that the folded state is stable, as it corresponds to a local minimum of the strain energy. Therefore, one can find from Figs. 14(b) and 14(c) that the folded configuration of the hexagonal ring with $h/t = 2$ is unstable, while that of the ring with $h/t = 5$ is stable. Folding processes of the hexagonal ring with a stable final configuration (i.e., $h/t = 5$) under twisting and bending loads are presented in Figs. 14(g) and 14(h), respectively. It can be observed that the hexagonal ring folds into the same peach core-shaped configuration even when undergoing different folding processes.

Regular ring origami with rectangular cross section can only be folded into a small-volume configuration under either bending or twisting loads. However, in large-scale applications, it is usually technically difficult to fold a structure through bending or twisting. Therefore, ring origami capable of folding through simpler folding methods, such as a point load, is desirable. Recently, Lu et al. [207] found that easier snap-folding of ring origami can be achieved by introducing two different types of geometric modifications to the ring. One modification is to induce residual strain, while the other is to create pre-twisted edges. It is shown that residual strain can reduce the required energy barrier to fold the ring, while the pre-twisted edges allow for easier out-of-plane deformation, which is a condition required for ring folding. The combination of these two modifications enables the snap-folding of ring origami under a point load or localized twist or squeeze. To demonstrate this, Figs. 14(d)–14(f) studies the folding behavior of a modified hexagonal ring with $h/t = 4$ and $r/a = 0.05$ under a point load [207], in which ε_0 denotes the residual strain on the surface of the ring, and γ is the pre-twisted angle at the two ends of each straight edge of the ring. As shown in Fig. 14(d), a point load P is applied at one corner of the hexagonal ring. When the ring
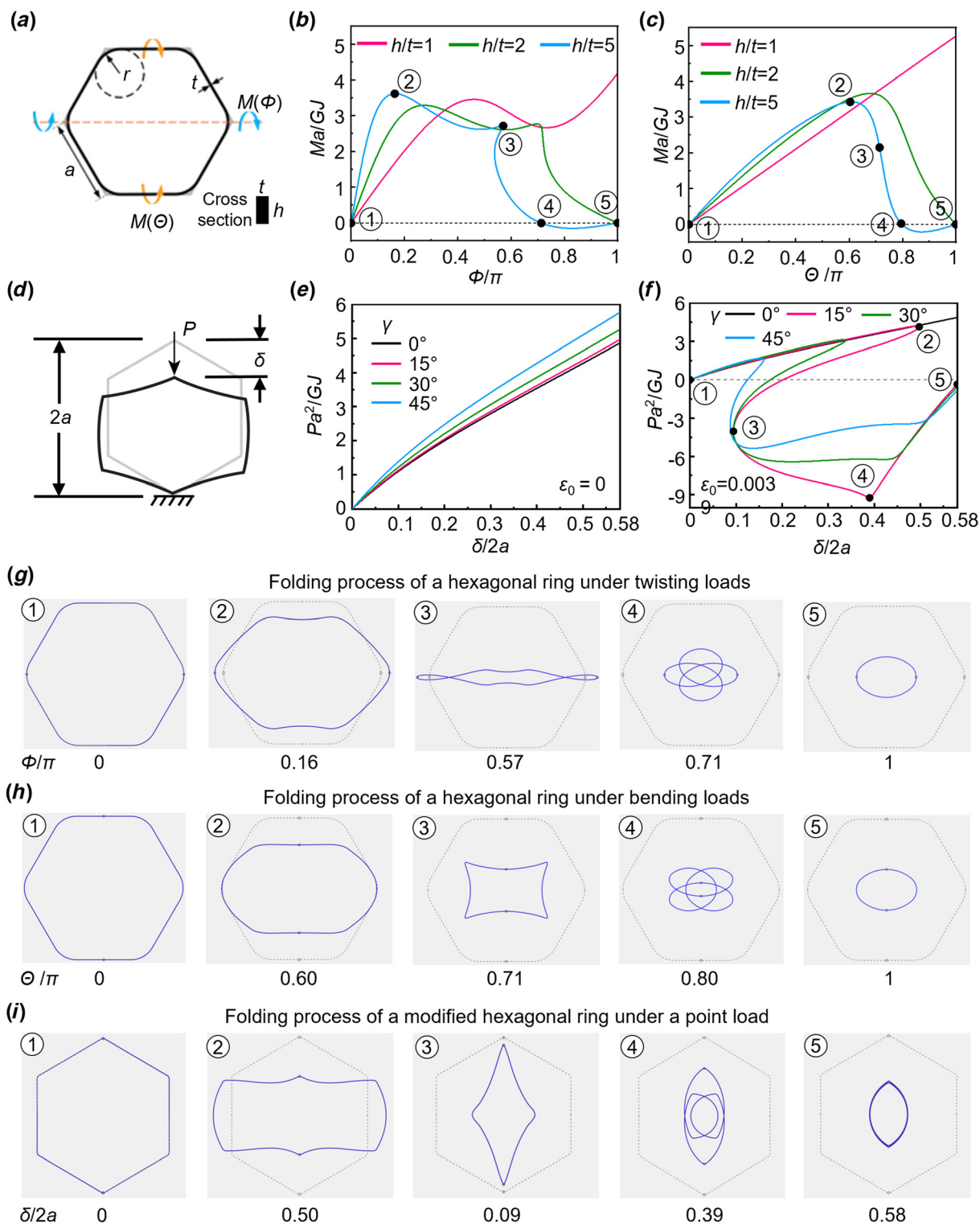
Fig. 14 Snap-folding behaviors of hexagonal rings. (*a*) Schematic of a hexagonal ring (*r*/*a* = 0.3) under bending or twisting loads. (*b*) Normalized moment-twisting angle curves for hexagonal rings with different height-to-thickness ratios (*h*/*t*) under twisting loads. (*c*) Normalized moment-bending angle curves for hexagonal rings with different height-to-thickness ratios (*h*/*t*) under bending loads. (*d*) Schematic of a hexagonal ring (*h*/*t* = 4, *r*/*a* = 0.05) under a point load [207]. (*e*) Normalized force–displacement curves for modified hexagonal rings with different pre-twisted angles of their edges under point loads [207]. (*f*) Normalized force–displacement curves for modified hexagonal rings with residual strain (ε_0=0.0039) and different pre-twisted angles of their edges under point loads [207]. (*g*) Folding process of a hexagonal ring with *h*/*t* = 5 and *r*/*a* = 0.3 under twisting loads. (*h*) Folding process of a hexagonal ring with *h*/*t* = 5 and *r*/*a* = 0.3 under bending loads. (*i*) Folding process of a modified hexagonal ring with *h*/*t* = 4, *r*/*a* = 0.05, residual strain (ε_0 = 0.0039), and pre-twisted edges (*γ* = 15 deg) under a point load. (Figures (*d*)–(*f*) and (*i*) are adapted with permission from Ref. [207]. Copyright 2022 by Elsevier).

has no geometric modifications ($\varepsilon_0 = 0$ and $\gamma = 0$) or has only pre-twisted edges and no residual strain ($\gamma \neq 0$ and $\varepsilon_0 = 0$), the force monotonically increases with the displacement δ (Fig. 14(e)), which means that the ring cannot fold under a point load in these conditions. However, when the ring has both residual strain and pre-twisted edges, the ring becomes foldable with the help of the snap-back instability. It is seen from Fig. 14(f) that the force first monotonically increases with the displacement. When the displacement reaches a critical value, snap-back takes place and helps the ring to fold to the final state. As the pre-twisted angle is increased, the critical displacement at which snap-back takes place gradually decreases. Figure 14(i) presents the folding process of a modified hexagonal ring under a point load [207]. It can be observed that the modified hexagonal ring snap-folds to a peach core shape like the regular hexagonal ring, but the modified ring can do so via a simple point load, benefitting from the easy folding enabled by geometric modifications.
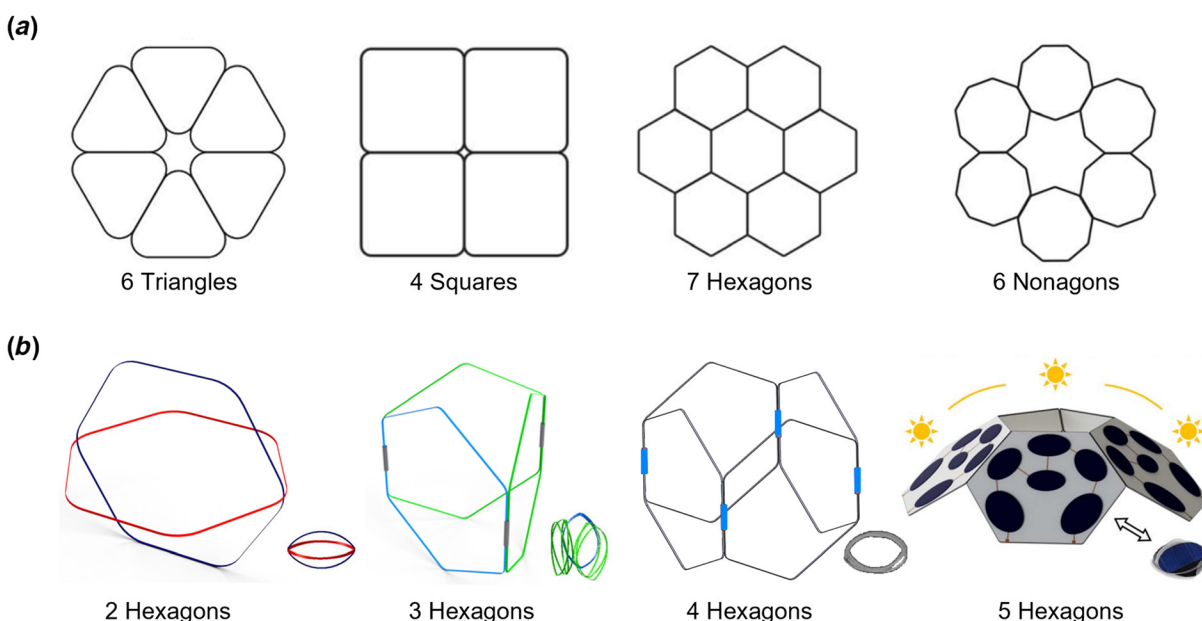
Ring origami can be tessellated or assembled to construct foldable structures with even more significant packing ratios than the individual rings [68,208]. Figure 15(a) shows four types of 2D tessellations composed of 6 triangular rings, 4 square rings, 7 hexagonal rings, and 6 nonagonal rings [208]. These ring tessellations can be folded into 2D small-volume configurations by first stacking all rings on top of one another and then applying bending or twisting moments. Among these tessellations, the hexagonal ring tessellation makes the most efficient use of space, as its tessellation is nearly gapless and its folded configuration is a multiloop overlapping state. Figure 15(b) presents four 3D ring systems constructed by assembling different numbers of hexagonal rings, which are a 2-ring assembly, a 3-ring assembly, a 4-ring assembly, and a 5-ring assembly, respectively [208]. The 2-ring and 3-ring assemblies can be directly folded into 3D small-volume configurations under bending or twisting loads, while the studied 4-ring and 5-ring assemblies first required stacking of all the rings to a 2D configuration, and then folding via application of bending or twisting loads. To fully take advantage of the folding capabilities of ring origami, rigid functional components can be integrated with ring origami assemblies via flexible membranes to enable functional devices. For example, the 5-ring dome-like assembly with thin membrane attached and strategically-placed solar panels based on the ring folding path could potentially serve as a deployable energy harvesting

structure [208], as shown in Fig. 15(b). Note that, when using modified hexagonal rings with residual strain and pre-twisted edges as the building blocks, ring origami tessellations and assemblies can be folded under point loads [207]. Therefore, ring origami can be a promising building block to construct easy-to-fold origami-based functional structures with impressive packing abilities.

6 Summary and Outlook

In this paper, we reviewed the recent works on origami with rotational symmetry and placed emphasis on their designs and mechanics. We classified origami with rotational symmetry into three categories according to the dimensional transitions between their deployed and folded states. For each category, we introduced the geometric designs of various origami patterns and discussed in detail their mechanical behaviors during the folding process. Although many achievements have been made in the study of origami with rotational symmetry, there remain numerous challenges. Here, we provide our views on the potential directions and future challenges.

- Various simulation methods have been developed to study mechanical behaviors of origami structures, while theoretical modeling in this aspect is relatively scarce. So far, most of the theoretical works on mechanical analysis of non-rigidly foldable origami have utilized the triangulated truss model, which does not capture panel deformation in a precise way. However, the elastic deformation of origami panels during folding has remarkable influences on the bistability, multistability, and energy storage characteristics as well as the energy landscapes of origami structures. Therefore, accurate theoretical modeling of the mechanical behaviors of origami structures to better guide the rational design of origami-based functional applications remains a challenge.
- Origami has been used to design deployable structures with target geometric shapes, while few works have focused on how to design origami structures, such as unit cell geometry and crease pattern distribution, to enable target mechanical properties including stiffness, stable states, energy landscapes, and energy absorption capacities, etc. For example, Kresling origami assemblies have shown the capability of tuning stiffness by selectively folding/unfolding the units.

(a)

6 Triangles   4 Squares   7 Hexagons   6 Nonagons

(b)

2 Hexagons   3 Hexagons   4 Hexagons   5 Hexagons

Fig. 15 Tessellations and assemblies of ring origami (Adapted with permission from Ref. [208]. Copyright 2022 by ASME). (a) 2D tessellations. From left to right: 6-triangular ring tessellation, 4-square ring tessellation, 7-hexagonal ring tessellation, and 6-nonagonal ring tessellation. (b) 3D assemblies of hexagonal rings and their corresponding folded states. From left to right: 2-ring assembly, 3-ring assembly, 4-ring assembly, and 5-ring schematic dome assembly with solar panels.

However, how to design Kresling origami with target stiffness remains unexplored. To address these problems, inverse design strategies are desired to be developed for origami structures to meet specific application requirements, which can be potentially achieved by using machine learning algorithms [209–211] and topology optimization [212–214].

- Origami-based metamaterials have been explored in recent years, while most works mainly focus on demonstrating tunable mechanical properties such as stiffness and Poisson's ratio. There are emerging works using the shape reconfiguration and multistability of origami to tune other physical properties and behaviors such as acoustic bandgaps [215–217], coefficients of thermal expansion [134,218], and electromagnetic wave propagation [219,220]. These multifunctional origami systems can broaden the application landscape of origami, and is worth further systematic study combined with inverse design strategy.

- In most current origami research, the materials used for demonstrating the folding mechanism of origami are largely based on papers or plastic sheets, which are less practical in real applications for foldable architectural structures, deployable biomedical devices, and deployable aerospace structures, etc. Moreover, the actuation method is mostly based on mechanical loading of tension, compression, bending, and torsion, which limits origami applications requiring wireless remote actuation. Therefore, it is important to explore different material options for desired mechanical properties and actuation strategies for functional origami. Particularly, origami integrated with active materials such as shape memory polymers [221,222], liquid crystal elastomers [223,224], and magnetic materials [225–227] which can self-fold under physical stimulation has great potential for advanced functional applications.

In summary, origami with rotational symmetry has been demonstrated to be a promising building block for the design of functional structures and devices. It is expected that the current review can help researchers better understand the mechanics and design of origami with rotational symmetry, and thus achieve more functional applications across a wide range of length scales.

Funding Data

Data Availability Statement

The datasets generated and supporting the findings of this article are obtainable from the corresponding author upon reasonable request.

References

[1] Callens, S. J., and Zadpoor, A. A., 2018, "From Flat Sheets to Curved Geometries: Origami and Kirigami Approaches," Mater. Today, 21(3), pp. 241–264.

[2] Silverberg, J. L., Na, J.-H., Evans, A. A., Liu, B., Hull, T. C., Santangelo, C. D., Lang, R. J., Hayward, R. C., and Cohen, I., 2015, "Origami Structures With a Critical Transition to Bistability Arising From Hidden Degrees of Freedom," Nat. Mater., 14(4), pp. 389–393.

[3] Cai, J., Deng, X., Zhou, Y., Feng, J., and Tu, Y., 2015, "Bistable Behavior of the Cylindrical Origami Structure With Kresling Pattern," ASME J. Mech. Des., 137(6), p. 061406.

[4] Faber, J. A., Arrieta, A. F., and Studart, A. R., 2018, "Bioinspired Spring Origami," Science, 359(6382), pp. 1386–1391.

[5] Liu, K., Tachi, T., and Paulino, G. H., 2019, "Invariant and Smooth Limit of Discrete Geometry Folded From Bistable Origami Leading to Multistable Metasurfaces," Nat. Commun., 10(1), pp. 1–10.

[6] Waitukaitis, S., Menaut, R., Chen, B. G.-G., and Van Hecke, M., 2015, "Origami Multistability: From Single Vertices to Metasheets," Phys. Rev. Lett., 114(5), p. 055503.

[7] Feng, F., Plucinsky, P., and James, R. D., 2020, "Helical Miura Origami," Phys. Rev. E, 101(3), p. 033002.

[8] Fang, H., Wang, K., and Li, S., 2017, "Asymmetric Energy Barrier and Mechanical Diode Effect From Folding Multi-Stable Stacked-Origami," Extreme Mech. Lett., 17, pp. 7–15.

[9] Wei, Z. Y., Guo, Z. V., Dudte, L., Liang, H. Y., and Mahadevan, L., 2013, "Geometric Mechanics of Periodic Pleated Origami," Phys. Rev. Lett., 110(21), p. 215501.

[10] Yasuda, H., and Yang, J., 2015, "Reentrant Origami-Based Metamaterials With Negative Poisson's Ratio and Bistability," Phys. Rev. Lett., 114(18), p. 185502.

[11] Kamrava, S., Mousanezhad, D., Ebrahimi, H., Ghosh, R., and Vaziri, A., 2017, "Origami-Based Cellular Metamaterial With Auxetic, Bistable, and Self-Locking Properties," Sci. Rep., 7(1), pp. 1–9.

[12] Mintchev, S., Shintake, J., and Floreano, D., 2018, "Bioinspired Dual-Stiffness Origami," Sci. Rob., 3(20), p. eaau0275.

[13] Jamalimehr, A., Mirzajanzadeh, M., Akbarzadeh, A., and Pasini, D., 2022, "Rigidly Flat-Foldable Class of Lockable Origami-Inspired Metamaterials With Topological Stiff States," Nat. Commun., 13(1), pp. 1–14.

[14] Lv, C., Krishnaraju, D., Konjevod, G., Yu, H., and Jiang, H., 2014, "Origami Based Mechanical Metamaterials," Sci. Rep., 4(1), pp. 1–6.

[15] Ma, J., Chai, S., and Chen, Y., 2022, "Geometric Design, Deformation Mode, and Energy Absorption of Patterned Thin-Walled Structures," Mech. Mater., 168, p. 104269.

[16] Yang, K., Xu, S., Shen, J., Zhou, S., and Xie, Y. M., 2016, "Energy Absorption of Thin-Walled Tubes With Pre-Folded Origami Patterns: Numerical Simulation and Experimental Verification," Thin-Walled Struct., 103, pp. 33–44.

[17] Filipov, E. T., Tachi, T., and Paulino, G. H., 2015, "Origami Tubes Assembled Into Stiff, yet Reconfigurable Structures and Metamaterials," Proc. Natl. Acad. Sci., 112(40), pp. 12321–12326.

[18] Li, S., Fang, H., Sadeghi, S., Bhovad, P., and Wang, K. W., 2019, "Architected Origami Materials: How Folding Creates Sophisticated Mechanical Properties," Adv. Mater., 31(5), p. 1805282.

[19] Melancon, D., Gorissen, B., García-Mora, C. J., Hoberman, C., and Bertoldi, K., 2021, "Multistable Inflatable Origami Structures at the Metre Scale," Nature, 592(7855), pp. 545–550.

[20] Reis, P. M., López Jiménez, F., and Marthelot, J., 2015, "Transforming Architectures Inspired by Origami," Proc. Natl. Acad. Sci., 112(40), pp. 12234–12235.

[21] Kuribayashi, K., Tsuchiya, K., You, Z., Tomus, D., Umemoto, M., Ito, T., and Sasaki, M., 2006, "Self-Deployable Origami Stent Grafts as a Biomedical Application of Ni-Rich TiNi Shape Memory Alloy Foil," Mater. Sci. Eng.: A, 419(1–2), pp. 131–137.

[22] Kim, S.-H., Lee, H. R., Yu, S. J., Han, M.-E., Lee, D. Y., Kim, S. Y., Ahn, H.-J., Han, M.-J., Lee, T.-I., Kim, T.-S., Kwon, S. K., Im, S. G., and Hwang, N. S., 2015, "Hydrogel-Laden Paper Scaffold System for Origami-Based Tissue Engineering," Proc. Natl. Acad. Sci., 112(50), pp. 15426–15431.

[23] Johnson, M., Chen, Y., Hovet, S., Xu, S., Wood, B., Ren, H., Tokuda, J., and Tse, Z. T. H., 2017, "Fabricating Biomedical Origami: A State-of-the-Art Review," Int. J. Comput. Assisted Radiology Surg., 12(11), pp. 2023–2032.

[24] Meloni, M., Cai, J., Zhang, Q., Sang-Hoon Lee, D., Li, M., Ma, R., Parashkevov, T. E., and Feng, J., 2021, "Engineering Origami: A Comprehensive Review of Recent Applications, Design Methods, and Tools," Adv. Sci., 8(13), p. 2000636.

[25] Rus, D., and Tolley, M. T., 2018, "Design, Fabrication and Control of Origami Robots," Nat. Rev. Mater., 3(6), pp. 101–112.

[26] Wu, S., Ze, Q., Dai, J., Udipi, N., Paulino, G. H., and Zhao, R., 2021, "Stretchable Origami Robotic Arm With Omnidirectional Bending and Twisting," Proc. Natl. Acad. Sci., 118(36), p. e2110023118.

[27] Kim, S.-J., Lee, D.-Y., Jung, G.-P., and Cho, K.-J., 2018, "An Origami-Inspired, Self-Locking Robotic Arm That Can Be Folded Flat," Sci. Rob., 3(16), p. eaar2915.

[28] Chen, Q., Feng, F., Lv, P., and Duan, H., 2022, "Origami Spring-Inspired Shape Morphing for Flexible Robotics," Soft Rob., 9(4), pp. 798–806.

[29] Felton, S., Tolley, M., Demaine, E., Rus, D., and Wood, R., 2014, "A Method for Building Self-Folding Machines," Science, 345(6197), pp. 644–646.

[30] Miyashita, S., Guitron, S., Ludersdorfer, M., Sung, C. R., and Rus, D., "An Untethered Miniature Origami Robot That Self-Folds, Walks, Swims, and Degrades," Proc. 2015 IEEE International Conference on Robotics and Automation (ICRA), Seattle, WA, May 26–30, pp. 1490–1496.

[31] Overvelde, J. T., De Jong, T. A., Shevchenko, Y., Becerra, S. A., Whitesides, G. M., Weaver, J. C., Hoberman, C., and Bertoldi, K., 2016, "A Three-Dimensional Actuated Origami-Inspired Transformable Metamaterial With Multiple Degrees of Freedom," Nat. Commun., 7(1), pp. 1–8.

[32] Liu, B., Silverberg, J. L., Evans, A. A., Santangelo, C. D., Lang, R. J., Hull, T. C., and Cohen, I., 2018, "Topological Kinematics of Origami Metamaterials," Nat. Phys., 14(8), pp. 811–815.

[33] Babaee, S., Overvelde, J. T., Chen, E. R., Tournat, V., and Bertoldi, K., 2016, "Reconfigurable Origami-Inspired Acoustic Waveguides," Sci. Adv., 2(11), p. e1601019.

[34] Zhai, Z., Wang, Y., Lin, K., Wu, L., and Jiang, H., 2020, "In Situ Stiffness Manipulation Using Elegant Curved Origami," Sci. Adv., 6(47), p. eabe2000.

[35] Silverberg, J. L., Evans, A. A., McLeod, L., Hayward, R. C., Hull, T., Santangelo, C. D., and Cohen, I., 2014, "Using Origami Design Principles to Fold Reprogrammable Mechanical Metamaterials," Science, 345(6197), pp. 647–650.

[36] Fang, H., Chu, S. C. A., Xia, Y., and Wang, K. W., 2018, "Programmable Self-Locking Origami Mechanical Metamaterials," Adv. Mater., 30(15), p. 1706311.

[37] Zhai, Z., Wu, L., and Jiang, H., 2021, "Mechanical Metamaterials Based on Origami and Kirigami," Appl. Phys. Rev., 8(4), p. 041319.

[38] Chen, T., Bilal, O. R., Lang, R., Daraio, C., and Shea, K., 2019, "Autonomous Deployment of a Solar Panel Using Elastic Origami and Distributed Shape-Memory-Polymer Actuators," Phys. Rev. Appl., **11**(6), p. 064069.

[39] Zirbel, S. A., Lang, R. J., Thomson, M. W., Sigel, D. A., Walkemeyer, P. E., Trease, B. P., Magleby, S. P., and Howell, L. L., 2013, "Accommodating Thickness in Origami-Based Deployable Arrays," ASME J. Mech. Des., **135**(11), p. 111005.

[40] Shah, S. I. H., and Lim, S., 2021, "Review on Recent Origami Inspired Antennas From Microwave to Terahertz Regime," Mater. Des., **198**, p. 109345.

[41] Xue, Z., Song, H., Rogers, J. A., Zhang, Y., and Huang, Y., 2020, "Mechanically-Guided Structural Designs in Stretchable Inorganic Electronics," Adv. Mater., **32**(15), p. 1902254.

[42] Shi, Y., Zhang, F., Nan, K., Wang, X., Wang, J., Zhang, Y., Zhang, Y., Luan, H., Hwang, K.-C., Huang, Y., Rogers, J. A., and Zhang, Y., 2017, "Plasticity-Induced Origami for Assembly of Three Dimensional Metallic Structures Guided by Compressive Buckling," Extreme Mech. Lett., **11**, pp. 105–110.

[43] Zhang, Y., Huang, Y., and Rogers, J. A., 2015, "Mechanics of Stretchable Batteries and Supercapacitors," Curr. Opin. Solid State Mater. Sci., **19**(3), pp. 190–199.

[44] Yan, Z., Han, M., Yang, Y., Nan, K., Luan, H., Luo, Y., Zhang, Y., Huang, Y., and Rogers, J. A., 2017, "Deterministic Assembly of 3D Mesostructures in Advanced Materials Via Compressive Buckling: A Short Review of Recent Progress," Extreme Mech. Lett., **11**, pp. 96–104.

[45] Ning, X., Wang, X., Zhang, Y., Yu, X., Choi, D., Zheng, N., Kim, D. S., Huang, Y., Zhang, Y., and Rogers, J. A., 2018, "Assembly of Advanced Materials Into 3D Functional Structures by Methods Inspired by Origami and Kirigami: A Review," Adv. Mater. Interfaces, **5**(13), p. 1800284.

[46] Yan, Z., Zhang, F., Wang, J., Liu, F., Guo, X., Nan, K., Lin, Q., Gao, M., Xiao, D., Shi, Y., Qiu, Y., Luan, H., Kim, J. H., Wang, Y., Luo, H., Han, M., Huang, Y., Zhang, Y., and Rogers, J. A., 2016, "Controlled Mechanical Buckling for Origami-Inspired Construction of 3D Microstructures in Advanced Materials," Adv. Funct. Mater., **26**(16), pp. 2629–2639.

[47] Kresling, B., 2008, "Natural Twist Buckling in Shells: From the Hawkmoth's Bellows to the Deployable Kresling-Pattern and Cylindrical Miura-Ori," Proceedings of the 6th International Conference on Computation of Shell and Spatial Structures IASS-IACM, Ithaca, NY, May 28–31, pp. 1–4.

[48] Chen, Y., Feng, H., Ma, J., Peng, R., and You, Z., 2016, "Symmetric Waterbomb Origami," Proc. R. Soc. A: Math., Phys. Eng. Sci., **472**(2190), p. 20150846.

[49] Kawasaki, T., and Yoshida, M., 1988, "Crystallographic Flat Origamis," Memoirs Faculty Sci., Kyushu Univ. Ser. A, Math., **42**(2), pp. 153–157.

[50] Ze, Q., Wu, S., Dai, J., Leanza, S., Ikeda, G., Yang, P. C., Iaccarino, G., and Zhao, R. R., 2022, "Spinning-Enabled Wireless Amphibious Origami Millirobot," Nat. Commun., **13**(1), p. 3118.

[51] Ze, Q., Wu, S., Nishikawa, J., Dai, J., Sun, Y., Leanza, S., Zemelka, C., Novelino, L. S., Paulino, G. H., and Zhao, R. R., 2022, "Soft Robotic Origami Crawler," Sci. Adv., **8**(13), p. eabm7834.

[52] Pagano, A., Yan, T., Chien, B., Wissa, A., and Tawfick, S., 2017, "A Crawling Robot Driven by Multi-Stable Origami," Smart Mater. Struct., **26**(9), p. 094007.

[53] Onal, C. D., Wood, R. J., and Rus, D., 2013, "An Origami-Inspired Approach to Worm Robots," IEEE/ASME Trans. Mechatronics, **18**(2), pp. 430–438.

[54] Lee, D.-Y., Kim, J.-K., Sohn, C.-Y., Heo, J.-M., and Cho, K.-J., 2021, "High–Load Capacity Origami Transformable Wheel," Sci. Rob., **6**(53), p. eabe0201.

[55] Lee, D.-Y., Kim, J.-S., Kim, S.-R., Koh, J.-S., and Cho, K.-J., 2013, "The Deformable Wheel Robot Using Magic-Ball Origami Structure," ASME Paper No. DETC2013-13016.

[56] Wilson, L., Pellegrino, S., and Danner, R., "Origami Sunshield Concepts for Space Telescopes," Proceedings of the 54th AIAA/ASME/ASCE/AHS/ASC Structures, Structural Dynamics, and Materials Conference, Boston, MA, Apr. 8–11, p. 1594.

[57] Guest, S., and Pellegrino, S., 1996, "A New Concept for Solid Surface Deployable Antennas," Acta Astronaut., **38**(2), pp. 103–113.

[58] Mahadevan, L., and Rica, S., 2005, "Self-Organized Origami," Science, **307**(5716), pp. 1740–1740.

[59] Kresling, B., 2012, "Origami-Structures in Nature: Lessons in Designing "Smart" Materials," MRS Online Proceedings Library (OPL), p. 1420.

[60] Kim, W., Byun, J., Kim, J.-K., Choi, W.-Y., Jakobsen, K., Jakobsen, J., Lee, D.-Y., and Cho, K.-J., 2019, "Bioinspired Dual-Morphing Stretchable Origami," Sci. Rob., **4**(36), p. eaay3493.

[61] Dudte, L. H., Choi, G. P., and Mahadevan, L., 2021, "An Additive Algorithm for Origami Design," Proc. Natl. Acad. Sci., **118**(21), p. e2019241118.

[62] Dieleman, P., Vasmel, N., Waitukaitis, S., and van Hecke, M., 2020, "Jigsaw Puzzle Design of Pluripotent Origami," Nat. Phys., **16**(1), pp. 63–68.

[63] Lang, R. J., 2012, *Origami Design Secrets: Mathematical Methods for an Ancient Art*, CRC Press, Boca Raton, FL.

[64] Demaine, E. D., and O'Rourke, J., 2007, *Geometric Folding Algorithms: Linkages, Origami, Polyhedra*, Cambridge University Press, New York.

[65] Brunck, V., Lechenault, F., Reid, A., and Adda-Bedia, M., 2016, "Elastic Theory of Origami-Based Metamaterials," Phys. Rev. E, **93**(3), p. 033005.

[66] Maden, F., Korkmaz, K., and Akgün, Y., 2011, "A Review of Planar Scissor Structural Mechanisms: Geometric Principles and Design Methods," Archit. Sci. Rev., **54**(3), pp. 246–257.

[67] Hanaor, A., and Levy, R., 2001, "Evaluation of Deployable Structures for Space Enclosures," Int. J. Space Struct., **16**(4), pp. 211–229.

[68] Wu, S., Yue, L., Jin, Y., Sun, X., Zemelka, C., Qi, H. J., and Zhao, R., 2021, "Ring Origami: Snap-Folding of Rings With Different Geometries," Adv. Intell. Syst., **3**(9), p. 2100107.

[69] Wu, S., Dai, J., Leanza, S., and Zhao, R. R., 2022, "Hexagonal Ring Origami—Snap-Folding With Large Packing Ratio," Extreme Mech. Lett., **53**, p. 101713.

[70] Yoshiaki, G., Yasuhito, W., Toshihiro, K., and Makoto, O., 1992, "Elastic Buckling Phenomenon Applicable to Deployable Rings," Int. J. Solids Struct., **29**(7), pp. 893–909.

[71] Yoshimura, Y., 1955, "On the Mechanism of Buckling of a Circular Cylindrical Shell Under Axial Compression," No. NACA-TM-1390.

[72] Tachi, T., 2009, "Generalization of Rigid-Foldable Quadrilateral-Mesh Origami," J. Int. Assoc. Shell Spatial Struct., **50**(3), pp. 173–179.

[73] Song, K., Zhou, X., Zang, S., Wang, H., and You, Z., 2017, "Design of Rigid-Foldable Doubly Curved Origami Tessellations Based on Trapezoidal Crease Patterns," Proc. R. Soc. A: Math., Phys. Eng. Sci., **473**(2200), p. 20170016.

[74] Resch, R. D., 1973, "The Topological Design of Sculptural and Architectural Systems," National Computer Conference and Exposition, New York, June 4–8, pp. 643–650.

[75] Demaine, E. D., Demaine, M. L., and Lubiw, A., 1999, "Polyhedral Sculptures With Hyperbolic Paraboloids," Proceedings of the 2nd Annual Conference of BRIDGES: Mathematical Connections in Art, Music, and Science (BRIDGES'99), Winfield, KS, July 30–Aug. 1, pp. 91–100.

[76] Masana, R., and Daqaq, M. F., 2019, "Equilibria and Bifurcations of a Foldable Paper-Based Spring Inspired by Kresling-Pattern Origami," Phys. Rev. E, **100**(6), p. 063001.

[77] Novelino, L. S., Ze, Q., Wu, S., Paulino, G. H., and Zhao, R., 2020, "Untethered Control of Functional Origami Microrobots With Distributed Actuation," Proc. Natl. Acad. Sci., **117**(39), pp. 24096–24101.

[78] Liu, K., and Paulino, G., 2017, "Nonlinear Mechanics of Non-Rigid Origami: An Efficient Computational Approach," Proc. R. Soc. A: Math., Phys. Eng. Sci., **473**(2206), p. 20170348.

[79] Suh, J.-E., Miyazawa, Y., Yang, J., and Han, J.-H., 2022, "Self-Reconfiguring and Stiffening Origami Tube," Adv. Eng. Mater., **24**(5), p. 2101202.

[80] Miura, K., and Tachi, T., 2010, "Synthesis of Rigid-Foldable Cylindrical Polyhedra," *Symmetry: Art and Science*, International Society for the Interdisciplinary Study of Symmetry, Gmuend, Austria, pp. 204–213.

[81] Cai, J., Deng, X., Xu, Y., and Feng, J., 2016, "Motion Analysis of a Foldable Barrel Vault Based on Regular and Irregular Yoshimura Origami," ASME J. Mech. Rob., **8**(2), p. 021017.

[82] Evans, T. A., Lang, R. J., Magleby, S. P., and Howell, L. L., 2015, "Rigidly Foldable Origami Gadgets and Tessellations," R. Soc. Open Sci., **2**(9), p. 150067.

[83] Reid, A., Lechenault, F., Rica, S., and Adda-Bedia, M., 2017, "Geometry and Design of Origami Bellows With Tunable Response," Phys. Rev. E, **95**(1), p. 013002.

[84] Kamrava, S., Ghosh, R., Wang, Z., and Vaziri, A., 2019, "Origami-Inspired Cellular Metamaterial With Anisotropic Multi-Stability," Adv. Eng. Mater., **21**(2), p. 1800895.

[85] Feng, H., Peng, R., Zang, S., Ma, J., and Chen, Y., 2020, "Rigid Foldability and Mountain-Valley Crease Assignments of Square-Twist Origami Pattern," Mech. Mach. Theory, **152**, p. 103947.

[86] Wang, L.-C., Song, W.-L., Fang, H., and Fang, D., 2022, "Reconfigurable Force–Displacement Profiles of the Square-Twist Origami," Int. J. Solids Struct., **241**, p. 111471.

[87] Lang, R. J., Magleby, S., and Howell, L., 2016, "Single Degree-of-Freedom Rigidly Foldable Cut Origami Flashers," ASME J. Mech. Rob., **8**(3), p. 031005.

[88] Guest, S. D., and Pellegrino, S., 1992, "Inextensional Wrapping of Flat Membranes," Proceedings of the First International Seminar on Structural Morphology, Montpellier, France, Sept. 7–11, pp. 203–215.

[89] Kumar, P., and Pellegrino, S., 2000, "Computation of Kinematic Paths and Bifurcation Points," Int. J. Solids Struct., **37**(46–47), pp. 7003–7027.

[90] Dudte, L. H., Vouga, E., Tachi, T., and Mahadevan, L., 2016, "Programming Curvature Using Origami Tessellations," Nat. Mater., **15**(5), pp. 583–588.

[91] Dang, X., Lu, L., Duan, H., and Wang, J., 2022, "Deployment Kinematics of Axisymmetric Miura Origami: Unit Cells, Tessellations, and Stacked Metamaterials," Int. J. Mech. Sci., **232**, p. 107615.

[92] Dang, X., Feng, F., Plucinsky, P., James, R. D., Duan, H., and Wang, J., 2022, "Inverse Design of Deployable Origami Structures That Approximate a General Surface," Int. J. Solids Struct., **234–235**, p. 111224.

[93] Filipov, E., and Redoutey, M., 2018, "Mechanical Characteristics of the Bistable Origami Hypar," Extreme Mech. Lett., **25**, pp. 16–26.

[94] You, Z., and Pellegrino, S., 1997, "Foldable Bar Structures," Int. J. Solids Struct., **34**(15), pp. 1825–1847.

[95] Roovers, K., and De Temmerman, N., 2017, "Deployable Scissor Grids Consisting of Translational Units," Int. J. Solids Struct., **121**, pp. 45–61.

[96] Hanna, B. H., Lund, J. M., Lang, R. J., Magleby, S. P., and Howell, L. L., 2014, "Waterbomb Base: A Symmetric Single-Vertex Bistable Origami Mechanism," Smart Mater. Struct., **23**(9), p. 094009.

[97] Filipov, E., Liu, K., Tachi, T., Schenk, M., and Paulino, G. H., 2017, "Bar and Hinge Models for Scalable Analysis of Origami," Int. J. Solids Struct., **124**, pp. 26–45.

[98] Gillman, A., Fuchi, K., and Buskohl, P., 2018, "Truss-Based Nonlinear Mechanical Analysis for Origami Structures Exhibiting Bifurcation and Limit Point Instabilities," Int. J. Solids Struct., **147**, pp. 80–93.

[99] Schenk, M., and Guest, S. D., 2011, "Origami Folding: A Structural Engineering Approach," Origami, **5**, pp. 291–304.

[100] Woodruff, S. R., and Filipov, E. T., 2020, "A Bar and Hinge Model Formulation for Structural Analysis of Curved-Crease Origami," Int. J. Solids Struct., **204–205**, pp. 114–127.

[101] Zhu, Y., Schenk, M., and Filipov, E. T., 2022, "A Review on Origami Simulations: From Kinematics, to Mechanics, Toward Multiphysics," ASME Appl. Mech. Rev., **74**(3), p. 030801.

[102] Kresling, B., 2020, "The Fifth Fold: Complex Symmetries in Kresling–Origami Patterns," Symmetry Culture Sci., **31**(4), pp. 403–416.

[103] Nayakanti, N., Tawfick, S. H., and Hart, A. J., 2018, "Twist-Coupled Kirigami Cells and Mechanisms," Extreme Mech. Lett., **21**, pp. 17–24.

[104] Yasuda, H., Miyazawa, Y., Charalampidis, E. G., Chong, C., Kevrekidis, P. G., and Yang, J., 2019, "Origami-Based Impact Mitigation Via Rarefaction Solitary Wave Creation," Sci. Adv., **5**(5), p. eaau2835.

[105] Kaufmann, J., Bhovad, P., and Li, S., 2022, "Harnessing the Multistability of Kresling Origami for Reconfigurable Articulation in Soft Robotic Arms," Soft Rob., **9**(2), pp. 212–223.

[106] Zhang, J., Zhang, L., and Wang, C., 2022, "Kresling Origami-Inspired Reconfigurable Antenna With Spherical Cap," Int. J. Mech. Sci., **227**, p. 107470.

[107] Liu, X., Yao, S., and Georgakopoulos, S. V., 2017, "Mode Reconfigurable Bistable Spiral Antenna Based on Kresling Origami," Proc. 2017 IEEE International Symposium on Antennas and Propagation & USNC/URSI National Radio Science Meeting, San Diego, CA, July 9–14, pp. 413–414.

[108] Yasuda, H., Tachi, T., Lee, M., and Yang, J., 2017, "Origami-Based Tunable Truss Structures for Non-Volatile Mechanical Memory Operation," Nat. Commun., **8**(1), pp. 1–7.

[109] Masana, R., Khazaaleh, S., Alhussein, H., Crespo, R., and Daqaq, M., 2020, "An Origami-Inspired Dynamically Actuated Binary Switch," Appl. Phys. Lett., **117**(8), p. 081901.

[110] Hunt, G. W., and Ario, I., 2005, "Twist Buckling and the Foldable Cylinder: An Exercise in Origami," Int. J. Non-Linear Mech., **40**(6), pp. 833–843.

[111] Zhai, Z., Wang, Y., and Jiang, H., 2018, "Origami-Inspired, on-Demand Deployable and Collapsible Mechanical Metamaterials With Tunable Stiffness," Proc. Natl. Acad. Sci., **115**(9), pp. 2032–2037.

[112] Li, Z., Kidambi, N., Wang, L., and Wang, K.-W., 2020, "Uncovering Rotational Multifunctionalities of Coupled Kresling Modular Structures," Extreme Mech. Lett., **39**, p. 100795.

[113] Zhang, Q., Wang, X., Cai, J., and Feng, J., 2021, "Motion Paths and Mechanical Behavior of Origami-Inspired Tunable Structures," Mater. Today Commun., **26**, p. 101872.

[114] Kidambi, N., and Wang, K., 2020, "Dynamics of Kresling Origami Deployment," Phys. Rev. E, **101**(6), p. 063003.

[115] Agarwal, V., and Wang, K., 2022, "On the Nonlinear Dynamics of a Kresling-Pattern Origami Under Harmonic Force Excitation," Extreme Mech. Lett., **52**, p. 101653.

[116] Ishida, S., Uchida, H., Shimosaka, H., and Hagiwara, I., 2017, "Design and Numerical Analysis of Vibration Isolators With Quasi-Zero-Stiffness Characteristics Using Bistable Foldable Structures," ASME J. Vib. Acoust., **139**(3), p. 031015.

[117] Yang, X., and Keten, S., 2021, "Multi-Stability Property of Magneto-Kresling Truss Structures," ASME J. Appl. Mech., **88**(9), p. 091009.

[118] Lu, L., Dang, X., Feng, F., Lv, P., and Duan, H., 2022, "Conical Kresling Origami and Its Applications to Curvature and Energy Programming," Proc. R. Soc. A, **478**(2257), p. 20210712.

[119] Ishida, S., Nojima, T., and Hagiwara, I., 2014, "Mathematical Approach to Model Foldable Conical Structures Using Conformal Mapping," ASME J. Mech. Design, **136**(9), p. 091007.

[120] Sharma, H., and Upadhyay, S. H., 2020, "Geometric Design and Deployment Behavior of Origami Inspired Conical Structures," Mech. Based Des. Struct. Mach., pp. 1–25.

[121] Ishida, S., Nojima, T., and Hagiwara, I., 2015, "Regular Folding Pattern for Deployable Nonaxisymmetric Tubes," ASME J. Mech. Des., **137**(9), p. 091402.

[122] Al-Mulla, T., and Buehler, M. J., 2015, "Folding Creases Through Bending," Nat. Mater., **14**(4), pp. 366–368.

[123] Sharma, H., and Upadhyay, S., 2022, "Deployable Toroidal Structures Based on Modified Kresling Pattern," Mech. Mach. Theory, **176**, p. 104972.

[124] Melancon, D., Forte, A. E., Kamp, L. M., Gorissen, B., and Bertoldi, K., 2022, "Inflatable Origami: Multimodal Deformation Via Multistability," Adv. Funct. Mater., **32**(35), p. 2201891.

[125] Suh, J.-E., Kim, T.-H., and Han, J.-H., 2021, "New Approach to Folding a Thin-Walled Yoshimura Patterned Cylinder," J. Spacecr. Rockets, **58**(2), pp. 516–530.

[126] Zhang, Q., Fang, H., and Xu, J., 2021, "Yoshimura-Origami Based Earthworm-Like Robot With 3-Dimensional Locomotion Capability," Front. Rob. AI, **8**, p. 738214.

[127] Paez, L., Agarwal, G., and Paik, J., 2016, "Design and Analysis of a Soft Pneumatic Actuator With Origami Shell Reinforcement," Soft Rob., **3**(3), pp. 109–119.

[128] Chen, B., Shao, Z., Xie, Z., Liu, J., Pan, F., He, L., Zhang, L., Zhang, Y., Ling, X., Peng, F., Yun, W., and Wen, L., 2021, "Soft Origami Gripper With Variable Effective Length," Adv. Intell. Syst., **3**(10), p. 2000251.

[129] Micheletti, A., Giannetti, I., Mattei, G., and Tiero, A., 2022, "Kinematic and Static Design of Rigid Origami Structures: Application to Modular Yoshimura Patterns," J. Archit. Eng., **28**(2), p. 04022009.

[130] De Temmerman, I. A. N., Mollaert, M., Van Mele, I. A. T., and De Laet, I. A. L., 2007, "Design and Analysis of a Foldable Mobile Shelter System," Int. J. Space Struct., **22**(3), pp. 161–168.

[131] Foster, C., and Krishnakumar, S., 1987, "A Class of Transportable Demountable Structures," Int. J. Space Struct., **2**(3), pp. 129–137.

[132] Miura, K., 1985, "Method of Packaging and Deployment of Large Membranes in Space," Inst. Space Astronaut. Sci. Rep., **618**, pp. 1–9.

[133] Schenk, M., and Guest, S. D., 2013, "Geometry of Miura-Folded Metamaterials," Proc. Natl. Acad. Sci., **110**(9), pp. 3276–3281.

[134] Boatti, E., Vasios, N., and Bertoldi, K., 2017, "Origami Metamaterials for Tunable Thermal Expansion," Adv. Mater., **29**(26), p. 1700360.

[135] Li, S., Vogt, D. M., Rus, D., and Wood, R. J., 2017, "Fluid-Driven Origami-Inspired Artificial Muscles," Proc. Natl. Acad. Sci., **114**(50), pp. 13132–13137.

[136] Song, Z., Ma, T., Tang, R., Cheng, Q., Wang, X., Krishnaraju, D., Panat, R., Chan, C. K., Yu, H., and Jiang, H., 2014, "Origami Lithium-Ion Batteries," Nat. Commun., **5**(1), pp. 1–6.

[137] Tang, R., Huang, H., Tu, H., Liang, H., Liang, M., Song, Z., Xu, Y., Jiang, H., and Yu, H., 2014, "Origami-Enabled Deformable Silicon Solar Cells," Appl. Phys. Lett., **104**(8), p. 083501.

[138] Zhou, X., Wang, H., and You, Z., 2015, "Design of Three-Dimensional Origami Structures Based on a Vertex Approach," Proc. R. Soc. A: Math., Phys. Eng. Sci., **471**(2181), p. 20150407.

[139] Schenk, M., Kerr, S., Smyth, A., and Guest, S., 2013, "Inflatable Cylinders for Deployable Space Structures," Proc. First Conference Transformables, Seville, Spain, Sept. 18–20, pp. 1–6.

[140] Cai, J., Deng, X., Feng, J., and Zhou, Y., 2015, "Geometric Design and Mechanical Behavior of a Deployable Cylinder With Miura Origami," Smart Mater. Struct., **24**(12), p. 125031.

[141] Nojima, T., 2002, "Modelling of Folding Patterns in Flat Membranes and Cylinders by Origami," JSME Int. J. Ser. C Mech. Syst., Mach. Elem. Manuf., **45**(1), pp. 364–370.

[142] Bös, F., Wardetzky, M., Vouga, E., and Gottesman, O., 2017, "On the Incompressibility of Cylindrical Origami Patterns," ASME J. Mech. Des., **139**(2), p. 021404.

[143] Wang, F., Gong, H., Chen, X., and Chen, C., 2016, "Folding to Curved Surfaces: A Generalized Design Method and Mechanics of Origami-Based Cylindrical Structures," Sci. Rep., **6**(1), pp. 1–10.

[144] Du, Y., Keller, T., Song, C., Xiao, Z., Wu, L., and Xiong, J., 2021, "Design and Foldability of Miura-Based Cylindrical Origami Structures," Thin-Walled Struct., **159**, p. 107311.

[145] Sharma, H., and Upadhyay, S. H., 2021, "Folding Pattern Design and Deformation Behavior of Origami Based Conical Structures," Adv. Space Res., **67**(7), pp. 2058–2076.

[146] Lyu, S., Qin, B., Deng, H., and Ding, X., 2021, "Origami-Based Cellular Mechanical Metamaterials With Tunable Poisson's Ratio: Construction and Analysis," Int. J. Mech. Sci., **212**, p. 106791.

[147] Greenberg, H., Gong, M., Magleby, S., and Howell, L., 2011, "Identifying Links Between Origami and Compliant Mechanisms," Mech. Sci., **2**(2), pp. 217–225.

[148] Evans, T. A., Lang, R. J., Magleby, S. P., and Howell, L. L., 2015, "Rigidly Foldable Origami Twists," Origami, **6**(1), pp. 119–130.

[149] Wang, L.-C., Song, W.-L., and Fang, D., 2019, "Twistable Origami and Kirigami: From Structure-Guided Smartness to Mechanical Energy Storage," ACS Appl. Mater. Interfaces, **11**(3), pp. 3450–3458.

[150] Kamrava, S., Ghosh, R., Xiong, J., Felton, S. M., and Vaziri, A., 2019, "Origami-Equivalent Compliant Mechanism," Appl. Phys. Lett., **115**(17), p. 171904.

[151] Wang, L. C., Song, W. L., Zhang, Y. J., Qu, M. J., Zhao, Z., Chen, M., Yang, Y., Chen, H., and Fang, D., 2020, "Active Reconfigurable Tristable Square-Twist Origami," Adv. Funct. Mater., **30**(13), p. 1909087.

[152] Chen, Y., Peng, R., and You, Z., 2015, "Origami of Thick Panels," Science, **349**(6246), pp. 396–400.

[153] Lang, R. J., Tolman, K. A., Crampton, E. B., Magleby, S. P., and Howell, L. L., 2018, "A Review of Thickness-Accommodation Techniques in Origami-Inspired Engineering," ASME Appl. Mech. Rev., **70**(1), p. 010805.

[154] Wang, S., Gao, Y., Huang, H., Li, B., Guo, H., and Liu, R., 2022, "Design of Deployable Curved-Surface Rigid Origami Flashers," Mech. Mach. Theory, **167**, p. 104512.

[155] Morgan, J., Magleby, S. P., and Howell, L. L., 2016, "An Approach to Designing Origami-Adapted Aerospace Mechanisms," ASME J. Mech. Des., **138**(5), p. 052301.

[156] Guang, C., and Yang, Y., 2018, "An Approach to Designing Deployable Mechanisms Based on Rigid Modified Origami Flashers," ASME J. Mech. Des., **140**(8), p. 082301.

[157] Bowen, L., Springsteen, K., Feldstein, H., Frecker, M., Simpson, T. W., and von Lockette, P., 2015, "Development and Validation of a Dynamic Model of Magneto-Active Elastomer Actuation of the Origami Waterbomb Base," ASME J. Mech. Rob., **7**(1), p. 011010.

[158] Sadeghi, S., and Li, S., 2020, "Dynamic Folding of Origami by Exploiting Asymmetric bi-Stability," Extreme Mech. Lett., **40**, p. 100958.

[159] Treml, B., Gillman, A., Buskohl, P., and Vaia, R., 2018, "Origami Mechanologic," Proc. Natl. Acad. Sci., **115**(27), pp. 6916–6921.

[160] Meng, Z., Chen, W., Mei, T., Lai, Y., Li, Y., and Chen, C., 2021, "Bistability-Based Foldable Origami Mechanical Logic Gates," Extreme Mech. Lett., **43**, p. 101180.

[161] Li, S., Stampfli, J. J., Xu, H. J., Malkin, E., Diaz, E. V., Rus, D., and Wood, R. J., 2019, "A Vacuum-Driven Origami "Magic-Ball" Soft Gripper," Proc. 2019 International Conference on Robotics and Automation (ICRA), Montreal, QC, Canada, May 20–24, pp. 7401–7408.

[162] Fang, H., Zhang, Y., and Wang, K., 2017, "Origami-Based Earthworm-Like Locomotion Robots," Bioinspir. Biomim., **12**(6), p. 065003.

[163] Farnham, J., Hull, T. C., and Rumbolt, A., 2022, "Rigid Folding Equations of Degree-6 Origami Vertices," Proc. R. Soc. A, **478**(2260), p. 20220051.

[164] Fonseca, L. M., and Savi, M. A., 2021, "On the Symmetries of the Origami Waterbomb Pattern: Kinematics and Mechanical Investigations," Meccanica, **56**(10), pp. 2575–2598.

[165] Ma, J., Feng, H., Chen, Y., Hou, D., and You, Z., 2020, "Folding of Tubular Waterbomb," Res., **2020**, pp. 1–8.

[166] Imada, R., and Tachi, T., 2022, "Geometry and Kinematics of Cylindrical Waterbomb Tessellation," ASME J. Mech. Rob., **14**(4), p. 041009.

[167] Dong, S., Zhao, X., and Yu, Y., 2021, "Dynamic Unfolding Process of Origami Tessellations," Int. J. Solids Struct., **226–227**, p. 111075.

[168] Zhao, Y., Endo, Y., Kanamori, Y., and Mitani, J., 2018, "Approximating 3D Surfaces Using Generalized Waterbomb Tessellations," J. Comput. Des. Eng., **5**(4), pp. 442–448.

[169] Zhao, Y., Li, S., Zhang, M., Zeng, L., Yang, Y., Kanamori, Y., and Mitani, J., 2021, "Computational Design Methods for Cylindrical and Axisymmetric Waterbomb Tessellations," Comput. Aided Geometric Des., **91**, p. 102037.

[170] Tang, J., Tian, M., Wang, C., Wang, X., and Mao, H., 2021, "A Novel Scheme of Folding Discretized Surfaces of Revolution Inspired by Waterbomb Origami," Mech. Mach. Theory, **165**, p. 104431.

[171] Hu, Y., Zhou, Y., and Liang, H., 2021, "Constructing Rigid-Foldable Generalized Miura-Ori Tessellations for Curved Surfaces," ASME J. Mech. Rob., **13**(1), p. 011017.

[172] Feng, F., Dang, X., James, R. D., and Plucinsky, P., 2020, "The Designs and Deformations of Rigidly and Flat-Foldable Quadrilateral Mesh Origami," J. Mech. Phys. Solids, **142**, p. 104018.

[173] Hu, Y., Liang, H., and Duan, H., 2019, "Design of Cylindrical and Axisymmetric Origami Structures Based on Generalized Miura-Ori Cell," ASME J. Mech. Rob., **11**(5), p. 051004.

[174] Tachi, T., 2013, "Designing Freeform Origami Tessellations by Generalizing Resch's Patterns," ASME J. Mech. Design, **135**(11), p. 111006.

[175] Magliozzi, L., Micheletti, A., Pizzigoni, A., and Ruscica, G., 2017, "On the Design of Origami Structures With a Continuum of Equilibrium Shapes," Compos. Part B: Eng., **115**, pp. 144–150.

[176] Chen, Z., Wu, T., Nian, G., Shan, Y., Liang, X., Jiang, H., and Qu, S., 2019, "Ron Resch Origami Pattern Inspired Energy Absorption Structures," ASME J. Appl. Mech., **86**(1), p. 011005.

[177] Kshad, M. A. E., Popinigis, C., and Naguib, H. E., 2019, "3D Printing of Ron-Resch-Like Origami Cores for Compression and Impact Load Damping," Smart Mater. Struct., **28**(1), p. 015027.

[178] Seffen, K. A., 2012, "Compliant Shell Mechanisms," Philosophical Transactions of the Royal Society A: Mathematical," Phys. Eng. Sci., **370**(1965), pp. 2010–2026.

[179] Demaine, E. D., Demaine, M. L., Hart, V., Price, G. N., and Tachi, T., 2011, ("Non) Existence of Pleated Folds: How Paper Folds Between Creases," Graphs Combi., **27**(3), pp. 377–397.

[180] Yao, S., and Georgakopoulos, S. V., 2018, "Origami Segmented Helical Antenna With Switchable Sense of Polarization," IEEE Access, **6**, pp. 4528–4536.

[181] Liu, A., Johnson, M., and Sung, C., 2022, "Increasing Reliability of Self-Folding of the Origami Hypar," ASME J. Mech. Rob., **14**(6), p. 061003.

[182] Buhl, T., Jensen, F. V., and Pellegrino, S., 2004, "Shape Optimization of Cover Plates for Retractable Roof Structures," Comput. Struct., **82**(15–16), pp. 1227–1236.

[183] Mira, L. A., Thrall, A. P., and De Temmerman, N., 2014, "Deployable Scissor Arch for Transitional Shelters," Autom. Constr., **43**, pp. 123–131.

[184] Escrig, F., and Valcarcel, J. P., 1993, "Geometry of Expandable Space Structures," Int. J. Space Struct., **8**(1–2), pp. 71–84.

[185] Piñero, E. P., 1961, "Project for a Mobile Theatre," Archit. Des., **12**(1), pp. 154–155.

[186] Roovers, K., and Temmerman, N. D., 2015, "Digital Design of Deployable Scissor Grids Based on Circle Packing," Proceedings of IASS Annual Symposia, International Association for Shell and Spatial Structures (IASS), Amsterdam, The Netherlands, Aug. 17–20, pp. 1–12.

[187] Tsuda, S., Kohno, J., Nakahara, Y., and Ohsaki, M., 2022, "Composition of Curvilinearly Extendable Tubular Scissor Mechanisms," Int. J. Solids Struct., **250**, p. 111673.

[188] Roovers, K., and De Temmerman, N., 2017, "Geometric Design of Deployable Scissor Grids Consisting of Generalized Polar Units," J. Int. Assoc. Shell Spat. Struct., **58**(3), pp. 227–238.

[189] Han, B., Xu, Y., Yao, J., Zheng, D., Li, Y., and Zhao, Y., 2019, "Design and Analysis of a Scissors Double-Ring Truss Deployable Mechanism for Space Antennas," Aerosp. Sci. Technol., **93**, p. 105357.

[190] You, Z., and Pellegrino, S., 1997, "Cable-Stiffened Pantographic Deployable Structures Part 2: Mesh Reflector," AIAA J., **35**(8), pp. 1348–1355.

[191] Garcia-Mora, C. J., and Sanchez-Sanchez, J., 2021, "Limitations in the Design of Deployable Structures With Straight Scissors Using Identical Elements," Int. J. Solids Struct., **230**, p. 111171.

[192] Escrig, F., Sanchez, J., and Valcarcel, J. P., 1996, "Two Way Deployable Spherical Grids," Int. J. Space Struct., **11**(1–2), pp. 257–274.

[193] Zhao, P., Liu, J., Wu, C., Li, Y., and Chen, K., 2020, "Novel Surface Design of Deployable Reflector Antenna Based on Polar Scissor Structures," Chin. J. Mech. Eng., **33**(1), pp. 1–15.

[194] Hoberman, C., 1990, "Reversibly Expandable Doubly-Curved Truss Structure," U.S. Patent No. 4,942,700.

[195] Hoberman, C., 1991, "Radial Expansion/Retraction Truss Structures," U.S. Patent No. 5,024,031.

[196] Dinevari, N. F., Shahbazi, Y., and Maden, F., 2021, "Geometric and Analytical Design of Angulated Scissor Structures," Mech. Mach. Theory, **164**, p. 104402.

[197] Patel, J., and Ananthasuresh, G., 2007, "A Kinematic Theory for Radially Foldable Planar Linkages," Int. J. Solids Struct., **44**(18–19), pp. 6279–6298.

[198] Kiper, G., Söylemez, E., and Kişisel, A. Ö., 2008, "A Family of Deployable Polygons and Polyhedra," Mechanism Mach. Theory, **43**(5), pp. 627–640.

[199] Hoberman, C., 2013, "Mechanical Invention Through Computation-Mechanism Basics," MIT Class, **6**, p. S080.

[200] Krishnan, S., and Liao, Y., 2020, "Geometric Design of Deployable Spatial Structures Made of Three-Dimensional Angulated Members," J. Archit. Eng., **26**(3), p. 04020029.

[201] Pai, Pand., and Palazotto, A., 1996, "Large-Deformation Analysis of Flexible Beams," Int. J. Solids Struct., **33**(9), pp. 1335–1353.

[202] Audoly, B., and Seffen, K. A., 2016, "Buckling of Naturally Curved Elastic Strips: The Ribbon Model Makes a Difference," The Mechanics of Ribbons and Möbius Bands, Springer, Dordrecht, The Netherlands, pp. 293–320.

[203] Pellegrino, S., 2001, "Deployable Structures in Engineering," Deployable Structures, Springer, Vienna, Austria, pp. 1–35.

[204] Mouthuy, P.-O., Coulombier, M., Pardoen, T., Raskin, J.-P., Jonas,., and A., and M., 2012, "Overcurvature Describes the Buckling and Folding of Rings From Curved Origami to Foldable Tents," Nat. Commun., **3**(1), pp. 1–8.

[205] Yan, Z., Wang, K., and Wang, B., 2022, "Buckling of Circular Rings and Its Applications in Thin-Film Electronics," Int. J. Mech. Sci., **228**, p. 107477.

[206] Sun, X., Wu, S., Dai, J., Leanza, S., Yue, L., Yu, L., Jin, Y., Qi, H. J., and Zhao, R. R., 2022, "Phase Diagram and Mechanics of Snap-Folding of Ring Origami by Twisting," Int. J. Solids Struct., **248**, p. 111685.

[207] Lu, L., Leanza, S., Dai, J., Sun, X., and Zhao, R. R., 2023, "Easy Snap-Folding of Hexagonal Ring Origami by Geometric Modifications," J. Mech. Phys. Solids, **171**, p. 105142.

[208] Leanza, S., Wu, S., Dai, J., and Zhao, R. R., 2022, "Hexagonal Ring Origami Assemblies? Foldable Functional Structures With Extreme Packing," ASME J. Appl. Mech., **89**(8), pp. 1–20.

[209] Ma, C., Chang, Y., Wu, S., and Zhao, R. R., 2022, "Deep Learning-Accelerated Designs of Tunable Magneto-Mechanical Metamaterials," ACS Appl. Mater. Interfaces, **14**(29), pp. 33892–33902.

[210] Sun, X., Yue, L., Yu, L., Shao, H., Peng, X., Zhou, K., Demoly, F., Zhao, R., and Qi, H. J., 2022, "Machine Learning-Evolutionary Algorithm Enabled Design for 4D-Printed Active Composite Structures," Adv. Funct. Mater., **32**(10), p. 2109805.

[211] Zhu, Y., and Filipov, E. T., 2022, "Harnessing Interpretable Machine Learning for Holistic Inverse Design of Origami," Sci. Rep., **12**(1), pp. 1–12.

[212] Fuchi, K., and Diaz, A. R., 2013, "Origami Design by Topology Optimization," ASME J. Mech. Des., **135**(11), p. 111003.

[213] Eschenauer, H. A., and Olhoff, N., 2001, "Topology Optimization of Continuum Structures: A Review," ASME Appl. Mech. Rev., **54**(4), pp. 331–390.

[214] Zhou, Y., Nomura, T., Dede, E. M., and Saitou, K., 2022, "Topology Optimization With Wall Thickness and Piecewise Developability Constraints for Foldable Shape-Changing Structures," Struct. Multidiscip. Optim., **65**(4), pp. 1–13.

[215] Pratapa, P. P., Suryanarayana, P., and Paulino, G. H., 2018, "Bloch Wave Framework for Structures With Nonlocal Interactions: Application to the Design of Origami Acoustic Metamaterials," J. Mech. Phys. Solids, **118**, pp. 115–132.

[216] Oudghiri-Idrissi, O., and Guzina, B. B., 2022, "Effective Linear Wave Motion in Periodic Origami Structures," Comput. Methods Appl. Mech. Eng., **399**, p. 115386.

[217] Xu, Z.-L., Wang, Y.-Q., Zhu, R., and Chuang, K.-C., 2021, "Torsional Bandgap Switching in Metamaterials With Compression–Torsion Interacted Origami Resonators," J. Appl. Phys., **130**(4), p. 045105.

[218] Zhang, C., Yang, Q., and Tao, R., 2021, "Origami-Based Metamaterial With Switchable Abnormal Expansion Function," Smart Mater. Struct., **30**(7), p. 075004.

[219] Wang, Z., Jing, L., Yao, K., Yang, Y., Zheng, B., Soukoulis, C. M., Chen, H., and Liu, Y., 2017, "Origami-Based Reconfigurable Metamaterials for Tunable Chirality," Adv. Mater., **29**(27), p. 1700412.

[220] Venkatesh, S., Sturm, D., Lu, X., Lang, R. J., and Sengupta, K., 2022, "Origami Microwave Imaging Array: Metasurface Tiles on a Shape-Morphing Surface for Reconfigurable Computational Imaging," Adv. Sci., **9**(28), p. 2105016.

[221] Ma, C., Wu, S., Ze, Q., Kuang, X., Zhang, R., Qi, H. J., and Zhao, R., 2021, "Magnetic Multimaterial Printing for Multimodal Shape Transformation With Tunable Properties and Shiftable Mechanical Behaviors," ACS Appl. Mater. Interfaces, **13**(11), pp. 12639–12648.

[222] Ze, Q., Kuang, X., Wu, S., Wong, J., Montgomery, S. M., Zhang, R., Kovitz, J. M., Yang, F., Qi, H. J., and Zhao, R., 2020, "Magnetic Shape Memory Polymers With Integrated Multifunctional Shape Manipulation," Adv. Mater., **32**(4), p. 1906657.

[223] Peng, X., Wu, S., Sun, X., Yue, L., Montgomery, S. M., Demoly, F., Zhou, K., Zhao, R. R., and Qi, H. J., 2022, "4D Printing of Freestanding Liquid Crystal Elastomers Via Hybrid Additive Manufacturing," Adv. Mater., **34**(39), p. 2204890.

[224] Roach, D. J., Sun, X., Peng, X., Demoly, F., Zhou, K., and Qi, H. J., 2022, "4D Printed Multifunctional Composites With Cooling-Rate Mediated Tunable Shape Morphing," Adv. Funct. Mater., **32**(36), p. 2203236.

[225] Kuang, X., Wu, S., Ze, Q., Yue, L., Jin, Y., Montgomery, S. M., Yang, F., Qi, H. J., and Zhao, R., 2021, "Magnetic Dynamic Polymers for Modular Assembling and Reconfigurable Morphing Architectures," Adv. Mater., **33**(30), p. 2102113.

[226] Montgomery, S. M., Wu, S., Kuang, X., Armstrong, C. D., Zemelka, C., Ze, Q., Zhang, R., Zhao, R., and Qi, H. J., 2021, "Magneto-Mechanical Metamaterials With Widely Tunable Mechanical Properties and Acoustic Bandgaps," Adv. Funct. Mater., **31**(3), p. 2005319.

[227] Wu, S., Eichenberger, J., Dai, J., Chang, Y., Ghalichechian, N., and Zhao, R. R., 2022, "Magnetically Actuated Reconfigurable Metamaterials as Conformal Electromagnetic Filters," Adv. Intell. Syst., **4**(9), p. 2200106.